

NACA RM SL54H24

AUG 20 1954 RECT

~~SECRET~~
~~CLASSIFICATION CANCELLED~~
Authority NASA PUBLICATIONS
ANNOUNCEMENTS NO. 29
Date 8/20/54 By [signature]

Restriction/Classification
Cancelled



RESEARCH MEMORANDUM

for the

U. S. Air Force

LONGITUDINAL STABILITY AND CONTROL CHARACTERISTICS

AT TRANSONIC SPEEDS OF A 1/30-SCALE MODEL OF

THE REPUBLIC XF-103 AIRPLANE

By Arvo A. Luoma

Langley Aeronautical Laboratory
Langley Field, Va.

~~CLASSIFICATION CANCELLED~~
This material contains information affecting the National Defense of the United States within the meaning of the espionage laws, Title 18, U.S.C., Secs. 793 and 794, the transmission or revelation of which in any manner to an unauthorized person is prohibited by law.

~~CLASSIFIED DOCUMENT~~
~~ANNOUNCEMENTS NO. 29~~
NATIONAL ADVISORY COMMITTEE
FOR AERONAUTICS

WASHINGTON

AUG 18 1954

FILE COPY

To be returned to
the files of the National
Advisory Committee
for Aeronautics
Washington, D.C.

14
CLASSIFICATION CANCELLED

on all pages

~~SECRET~~
~~CLASSIFICATION CANCELLED~~
Authority NASA PUBLICATIONS
ANNOUNCEMENTS NO. 29
Date 8/18/54 By [signature]

CLASSIFICATION CANCELLEDNATIONAL ADVISORY COMMITTEE FOR AERONAUTICS
ANNOUNCEMENTS NO.

Date _____ By _____

RESEARCH MEMORANDUM

for the

U. S. Air Force

LONGITUDINAL STABILITY AND CONTROL CHARACTERISTICS

AT TRANSONIC SPEEDS OF A 1/30-SCALE MODEL OF

THE REPUBLIC XF-103 AIRPLANE

By Arvo A. Luoma

SUMMARY

The longitudinal stability and control characteristics of a 1/30-scale model of the Republic XF-103 airplane were investigated in the Langley 8-foot transonic tunnel. The effect of speed brakes located at the end of the fuselage was also investigated. The main part of the investigation was made with internal flow in the model, but some data were obtained with no internal flow.

The longitudinal stability and control at transonic speeds appeared satisfactory. The transonic drag rise was small. The speed brakes had no adverse effects on longitudinal stability.

INTRODUCTION

Wind-tunnel investigations of the stability and control characteristics of the Republic XF-103 airplane have been made at low subsonic speeds (ref. 1) and at supersonic speeds (refs. 2 and 3). At the request of the U. S. Air Force, the stability and control characteristics of a 1/30-scale model of the Republic XF-103 airplane at high subsonic and transonic Mach numbers were investigated at the Langley Laboratory. The investigation at high subsonic Mach numbers was made in the Langley high-speed 7- by 10-foot tunnel and included tests of the longitudinal, lateral, and directional stability and control characteristics of the XF-103 airplane and of the characteristics of wing fences, wing tanks, and fuselage speed brakes; these results are reported in reference 4.

CLASSIFICATION CANCELLEDAuthority NACA PUBLICATIONS
ANNOUNCEMENTS NO.

Date _____ By _____

The investigation at transonic Mach numbers was made in the Langley 8-foot transonic tunnel and included tests of the longitudinal stability and control characteristics of the XF-103 airplane, of speed brake characteristics, and of internal-flow characteristics. These results are reported herein.

SYMBOLS

The term "complete model" as used herein refers to the combination of fuselage, wing, vertical tail, and horizontal tail. The center-of-gravity location about which aerodynamic moments were computed was on the reference line of the fuselage and 36.1 percent of the mean aerodynamic chord of the wing back from the leading edge of the mean aerodynamic chord. The symbols used in this paper are defined as follows:

A_b fuselage base area; total cross-sectional area of fuselage at end of fuselage

A_d duct exit area at end of fuselage

A_r fuselage rim area; area enclosed by inner and outer walls of fuselage at end of fuselage

A_s cross-sectional area of sting within fuselage

C_D external drag coefficient; value determined from gage drag coefficient and corrected for pressure and internal drag coefficients for model with internal flow ($C_{D_g} - C_{D_p} - C_{D_i}$) and for base drag coefficient for model with no internal flow ($C_{D_g} - C_{D_b}$)

C_{D_b} base drag coefficient; value determined from base pressure coefficient for model with no internal flow, $-P_b \frac{A_b}{S} \cos \alpha$

C_{D_g} gage (overall) drag coefficient; value determined from strain-gage balance data and corrected for weight tares but uncorrected for pressure and internal drag coefficients with internal flow in model and for base drag coefficient with no internal flow in model, Gage drag/ $q_0 S$

C_{D_i} internal drag coefficient, $\frac{m}{q_0 S} (V_0 - V_d \cos \alpha) - P_d \frac{A_d}{S} \cos \alpha$

- C_{D_p} pressure drag coefficient; value determined from pressure coefficient in balance chamber and at rim of fuselage with internal flow in model, $\left(-P_c \frac{A_s}{S} - P_r \frac{A_r}{S}\right)(\cos \alpha)$
- $C_{D_{min}}$ minimum external-drag coefficient
- ΔC_D rise in external-drag coefficient above minimum value $(C_D - C_{D_{min}})$
- C_L lift coefficient, $Lift/q_0 S$
- $C_{L_{C_{D_{min}}}}$ lift coefficient corresponding to minimum external-drag coefficient
- ΔC_L change in lift coefficient from value corresponding to minimum external-drag coefficient $(C_L - C_{L_{C_{D_{min}}}})$
- $(\Delta C_L)_i, (\Delta C_D)_i, (\Delta C_m)_i$ incremental coefficients due to internal flow; values determined from coefficients for configuration with internal flow minus corresponding coefficients for same configuration without internal flow (duct plug in inlet)
- $\frac{\Delta C_D}{(\Delta C_L)^2}$ drag-due-to-lift factor
- $\frac{dC_L}{d\alpha}$ derivative of lift coefficient with respect to angle of attack
- C_m pitching-moment coefficient, $Pitching\ moment/q_0 S c'$
- $\frac{dC_m}{dC_L}$ derivative of pitching-moment coefficient with respect to lift coefficient
- c' mean aerodynamic chord of wing
- c_t' mean aerodynamic chord of horizontal tail
- i_t incidence of horizontal tail; value measured by angle between plane of horizontal tail and reference line of fuselage
- M_0 Mach number of undisturbed stream

- m mass flow in model duct
- P_b base (end of fuselage) pressure coefficient when no internal flow in model, $\frac{P_r - P_o}{q_o}$
- P_c pressure coefficient within strain-gage-balance chamber, $\frac{P_c - P_o}{q_o}$
- P_d pressure coefficient of internal flow at model duct exit at end of fuselage, $\frac{P_d - P_o}{q_o}$
- P_r pressure coefficient at fuselage rim, $\frac{P_r - P_o}{q_o}$; it is assumed herein that $P_r = P_d$
- p_b static pressure at fuselage base with no internal flow in model
- p_c static pressure within strain-gage-balance chamber
- p_d static pressure of internal flow at model duct exit at end of fuselage
- p_o static pressure of undisturbed stream
- P_r static pressure at fuselage rim
- q_o dynamic pressure of undisturbed stream, $\frac{1}{2}\rho_o V_o^2$
- R Reynolds number, $\frac{\rho_o V_o c'}{\mu_o}$
- S area of wing, including portion within fuselage
- V_d velocity of internal flow at model duct exit at end of fuselage
- V_o velocity of undisturbed stream
- α angle of attack of model; value based on reference line of fuselage
- ϵ effective downwash angle in region of horizontal tail; value determined from tests of complete model and complete model less horizontal tail

μ_0 coefficient of viscosity in undisturbed stream
 ρ_0 mass density of undisturbed stream

APPARATUS AND METHODS

Tunnel

The tests were made in the Langley 8-foot transonic tunnel. This tunnel operates at a stagnation pressure approximately equal to atmospheric pressure. The tunnel throat is of dodecagonal cross section with axial slots located at the vertices of the twelve wall panels. The slotted design permits model testing at speeds through sonic velocity (refs. 5 and 6). Information on the design of the slotted test section of the Langley 8-foot transonic tunnel is given in reference 7 and on the calibration of the flow in this tunnel in reference 6.

Model and Balance

Model.- The Republic XF-103 airplane has triangular wing and tail surfaces, has a rectangular, supersonic scoop inlet with sweptback side walls located on the bottom of the fuselage, and has a fuselage with rectangular cross sections in the region adjacent to the fuselage base. The model used in the present investigation was a sting-supported, 1/30-scale model of the XF-103 airplane, and was the same model and sting used in the Langley high-speed 7- by 10-foot tunnel tests of reference 4. The geometric characteristics of the model are shown in figure 1, and a photograph of the model as installed in the Langley high-speed 7- by 10-foot tunnel is shown as figure 2. The wing fences shown in the photograph were not included on the configurations tested in the Langley 8-foot transonic tunnel. The sting support was of rectangular cross section.

The model was provided with internal ducting leading from the scoop inlet, and the internal flow was "dumped" around the sting within the fuselage at a location behind the strain-gage balance and approximately 5 inches from the end of the fuselage. The inlet was closed for some of the tests with a faired plug as shown in figure 3.

The model was constructed of steel, and the wing used in the tests in the Langley 8-foot transonic tunnel was of solid construction without any cut-outs for control surfaces. The solid wing and a wing equipped with ailerons and flaps were both investigated in the tests in the Langley high-speed 7- by 10-foot tunnel. The dimensions of the 45° speed brakes and their location on the sides of the fuselage are shown in figure 4. The same speed brakes were tested in two axial locations.

Balance.- A six-component strain-gage balance housed within the fuselage was used for determining the forces and moments on the model. The balance was positioned in the fuselage so that the moment center of the balance was on the reference line of the fuselage and 36.1 percent of the mean aerodynamic chord of the wing back from the leading edge of the mean aerodynamic chord. The moment center of the balance coincided with the center-of-gravity location shown in figure 1.

Test Procedure

Force and moment tests.- Aerodynamic forces and moments were determined from strain-gage readings. The fuselage alone and the complete model were investigated at an angle of attack of 0° both with and without internal flow at Mach numbers from 0.40 to 1.15. No attempt was made to regulate the internal mass flow except when the internal flow was completely sealed off with the duct plug shown in figure 3. The fuselage alone and the complete model with internal flow were also tested with a roughness strip on the fuselage at a model angle of attack of 0° at Mach numbers from 0.60 to 1.15. The roughness consisted of a 1/8-inch-wide strip of no. 60 carborundum grains shellacked to the fuselage $1\frac{3}{4}$ inches back from the nose of the fuselage.

Various configurations, all with internal flow in the model, were tested through an angle-of-attack range at four (generally) transonic Mach numbers. The complete model at horizontal-tail incidences of 0° and -5° , the complete model less horizontal tail, and the complete model plus speed brakes were investigated. The configurations tested and the angles of attack, Mach numbers, and other pertinent test conditions at which force and moment data were taken are given in table I. The pitch tests were made with the model horizontal (when $\alpha = 0^\circ$) in the tunnel, and the angle of attack of the model was varied by pivoting the sting in a vertical plane. The pivot axis of the sting was located approximately 79 inches downstream of the model center-of-gravity location given in figure 1.

The no-load angle of attack of the model was obtained with a pendulum-type attitude transmitter, which was calibrated against inclination (in a vertical plane). The attitude transmitter was housed in the extension of the model sting and was located approximately 60 inches downstream of the model center-of-gravity location. Flexibility under aerodynamic load of the balance, model sting, and sting extension between the model and the attitude-transmitter location required a correction to the attitude-transmitter reading to obtain the model angle of attack. The angle of sideslip was 0° for all test conditions.

The average Reynolds number of the present investigation is shown plotted against Mach number in figure 5.

Pressure tests.- Mass-flow measurements of the internal flow were made with a rake consisting of 26 total-head and four static tubes located 1/16 inch downstream from the end of the fuselage. The internal mass flow of the complete model ($i_t = 0^\circ$) at an angle of attack of 0° at Mach numbers from 0.40 to 1.15 and throughout the angle-of-attack range at a Mach number of 0.96 was determined. The internal mass flow of the complete model less horizontal tail throughout the angle-of-attack range at Mach numbers of 0.96, 0.98, 1.02, and 1.12 was also determined. Overall force and moment data were obtained during the mass-flow tests from strain-gage readings.

The static pressure within the strain-gage-balance chamber and at the base of the fuselage was measured for all configurations.

CORRECTIONS AND ACCURACY

Pressure Correction to Drag

No internal flow in model.- The drag coefficient C_D for the configurations with no internal flow in the model has been adjusted for the difference between the actual measured static pressure at the base of the fuselage and that in the undisturbed stream, so that the drag coefficient C_D corresponds to a static pressure at the base of the fuselage equal to that of the undisturbed stream.

Internal flow in model.- The pressure drag correction C_{D_p} applied to the gage drag coefficient C_{D_g} of the configurations with internal flow in the model (see "Symbols" section) is an adjustment for the deviation from the free-stream value of the static pressure in the balance chamber and at the rim of the fuselage base.

The external drag coefficient C_D of the configurations with internal flow in the model further includes the internal drag correction C_{D_i} but does not include the friction force between the internal flow and the sting within the fuselage (see description of internal ducting in "Apparatus and Methods" section). Estimations showed that neglect of this friction term was small and would tend to make the drag coefficient C_D presented herein too low by approximately 0.0005.

No corrections are included herein for the effects of internal flow on lift and pitching-moment coefficients.

Tunnel-Boundary Interference

Subsonic Mach numbers.- At subsonic Mach numbers, the interference effects of a tunnel boundary on the flow over a model in the test region near the center line of the tunnel have been made negligible by means of a slotted test section (ref. 6).

Supersonic Mach numbers.- Data are presented herein at supersonic Mach numbers of 1.02 and 1.13 (1.12 for complete model less horizontal tail) for various configurations through the angle-of-attack range, and at intermediate supersonic Mach numbers of 1.04 and 1.11 (1.10 for one configuration) for several configurations at an angle of attack of 0° .

The intensity of the tunnel boundary-reflected compression and expansion disturbances at a Mach number of 1.02 has been found to be weak, so that the boundary interference on the data presented herein at a Mach number of 1.02 was probably small. The boundary interference at a Mach number of 1.04 is believed to have been confined primarily to affecting the drag data. No data are presented herein between Mach numbers of 1.04 and 1.10, where the effects of boundary interference may have been large.

Schlieren photographs taken during the present investigation showed that, at a Mach number of 1.11 and at a model angle of attack of 0° , the reflection of the fuselage nose shock cleared the model base by several inches; some of the base pressure data, however, indicated that the influence of the reflected shock may have extended upstream to the model base.

The schlieren photographs also indicated that the reflection of the fuselage nose shock may have impinged on the vertical tail at angles of attack greater than approximately 11° at a Mach number of 1.13 and at angles of attack greater than approximately 8° at a Mach number of 1.12. The force and moment data at these conditions showed no evident irregularities, however, and all these data are presented herein.

No corrections have been made to the data presented herein for tunnel-boundary interference except to the extent of the partial correction for tunnel-boundary interference inherent in the base-pressure correction, which was based on the actual measured value of base static pressure.

Sting-Interference Corrections

No sting-interference corrections have been made to the data presented herein except to the extent of the partial correction for sting interference inherent in the base-pressure correction, which was based on the actual measured value of base static pressure.

Precision of Data

The accuracy of the angle of attack was approximately $\pm 0.1^\circ$. Inaccuracies in sting coupling connections inadvertently caused the angle of sideslip to be slightly different from an intended value of 0° .

The estimated maximum error in measured lift coefficient, pitching-moment coefficient, and gage drag coefficient C_{D_g} at angles of attack near 0° was ± 0.005 , ± 0.004 , and ± 0.0005 , respectively, at transonic speeds. The maximum error in corrected drag coefficient C_D of the configurations with internal flow in the model would be greater by the extent of the possible errors in the pressure and internal-drag corrections terms, and was estimated to be approximately ± 0.002 at angles of attack near 0° .

RESULTS AND DISCUSSION

Presentation of Results

Pressure results.- The internal drag coefficient C_{D_i} , which was determined only for the complete model at a horizontal incidence of 0° and for the complete model less horizontal tail, is shown plotted against Mach number at an angle of attack of 0° in figure 6(a) and against angle of attack at various Mach numbers in figure 6(b). The inlet mass-flow ratio was approximately 1.0 for the configurations with internal flow in the model.

The base-pressure coefficient with no internal flow in the model is presented in figure 7 for the fuselage alone plus duct plug and for the complete model plus duct plug.

Basic force and moment results.- The basic force and moment results for the various configurations are presented in figures 8 to 17, inclusive, and an index of these figures together with general information about the test conditions is given in table I.

The drag data for the configurations with no internal flow in the model are presented herein in terms of the gage drag coefficient C_{D_g} and the corrected drag coefficient C_D (see "Symbols" section).

The drag data for the configurations with internal flow in the model are presented herein in terms of the drag coefficients C_{D_g} and $C_{D_g} - C_{D_p}$ for all the configurations, and in terms of the drag coefficient C_D for the complete model at horizontal-tail incidences of 0° .

and -5° , the complete model less horizontal tail, and the fuselage alone. The assumption was made that the internal drag coefficient C_{D_i} (fig. 6) also applied for the complete model at a horizontal-tail incidence of -5° and for the fuselage alone.

Summary force and moment results.- Summary plots derived from the basic force and moment data are shown in figures 18 to 26, inclusive. Comparisons are made in the summary plots between the results from the present investigation and those on the same model and sting from the investigation in the Langley high-speed 7- by 10-foot tunnel (ref. 4). The speed-brake configuration of reference 4, for which results are shown herein, included wing fences and the mass-flow survey rake; the other configurations of reference 4 for which results are shown herein did not include the wing fences and the survey rake.

The gage drag coefficient C_{D_g} of the complete model with internal flow in the model presented in figure 21(a) and identified as 7- by 10-foot tunnel data was obtained during check tests, in which the pressure drag correction C_{D_p} was measured, in the investigation of reference 4. The corrected drag coefficient C_D of the complete model shown in figure 21(a) and identified as 7- by 10-foot tunnel data was determined from the C_{D_g} and C_{D_p} data obtained in the check tests of reference 4 and the C_{D_i} data obtained in the present investigation. The corrected drag coefficient C_D of the fuselage alone, shown in figure 21(a) and identified as 7- by 10-foot tunnel data, includes the corrections C_{D_p} and C_{D_i} of the present investigation.

The corrected drag coefficient C_D of the complete model with no internal flow in the model, presented in figure 21(b) and identified as 7- by 10-foot tunnel data, was obtained during the check tests of reference 4. The corrected drag coefficient C_D of the fuselage alone with no internal flow in the model, shown in figure 21(b) and identified as 7- by 10-foot tunnel data, includes the base pressure correction C_{D_b} of the present investigation.

The Reynolds number of the investigation of reference 4 was essentially the same as that of the present investigation.

Lift Characteristics

The variation of lift-curve slope with Mach number at lift coefficients of 0 and 0.4 are shown in figure 18 for the various configurations. Where the curves of lift against angle of attack were nonlinear, the slopes shown are the average values for lift coefficients from 0.1 below to 0.1 above the specified lift coefficient.

The maximum value of lift-curve slope at a lift coefficient of zero occurred at a Mach number of approximately 0.98 for the complete model and for the complete model less horizontal tail (fig. 18(a)). Addition of speed brakes to the complete model reduced the lift-curve slope at transonic speeds by approximately 5 percent.

The agreement of the data on lift-curve slope from the two Langley tunnels generally was not wholly satisfactory. The variation of lift coefficient with angle of attack obtained from the 7- by 10-foot high-speed tunnel tests usually deviated more from a linear relationship than did the corresponding data from the transonic tunnel tests, with the lift-curve slope at lift coefficients near zero being lower for the 7- by 10-foot high-speed tunnel results (fig. 18). The explanation for the differences in lift characteristics is not evident. Part of the differences possibly may be ascribed to the inaccuracies inherent in fairing and determining slopes where the variation of the parameters is nonlinear, to possible differences in the turbulence level of the two tunnels, and, at the highest subsonic Mach numbers, possibly to the effects of incipient choking at lifting conditions in the 7- by 10-foot high-speed tunnel.

Pitching-Moment Characteristics

The variation with Mach number of the longitudinal-stability derivative dC_m/dC_L for the various configurations is presented in figure 19 at lift coefficients of 0 and 0.4. The slopes shown are average values for lift coefficients from 0.1 below to 0.1 above the specified lift coefficient.

The pitching-moment-slope data from the two Langley tunnels generally showed good agreement for the various configurations (fig. 19). For the complete model, there was a rearward movement of the aerodynamic center at transonic speeds amounting to approximately 14 percent of the mean aerodynamic chord of the wing. The speed brakes generally reduced the extent of the rearward movement of the aerodynamic center at transonic speeds, and generally reduced the stability somewhat at supersonic speeds.

No serious pitch-up tendencies were evident for the complete model at the horizontal-tail incidences investigated, although a localized unstable break in pitching moment occurred at the lower transonic Mach numbers at high lift coefficients (figs. 13(c) and 14(c)). For the complete model less horizontal tail, the unstable break in pitching moment increased in magnitude and extended over a greater lift-coefficient range (fig. 15(c)).

The speed brakes in location 1 increased the trim lift coefficient by approximately 0.10 to 0.15, depending on Mach number (figs. 13(c) and

16(c)), and by twice those values with the brakes in location 2 (figs. 13(c) and 17(c)). The brakes did not appear to aggravate the unstable break in pitching moment except to the extent that the unstable break occurred at lower lift coefficients.

Horizontal-Tail Effectiveness

The horizontal-tail effectiveness $\Delta C_m / \Delta i_t$ for the complete model at lift coefficients of 0 and 0.4 is shown in figure 20 plotted against Mach number. The effectiveness derivative shown is the average slope between horizontal-tail incidences of 0° and -5° .

An increase in horizontal-tail effectiveness occurred at high subsonic Mach numbers. This increase was approximately 20 percent at a lift coefficient of zero and approximately 40 percent at a lift coefficient of 0.4. The data from the Langley tunnels appeared to be in satisfactory agreement.

Drag Characteristics

The internal drag coefficient C_{D_i} of the complete model at an angle of attack of 0° was essentially constant throughout the Mach number range (fig. 6(a)). Removal of the horizontal tail from the model had no effect on the internal drag coefficient within the accuracy of the measurements (fig. 6). The internal drag coefficient increased to a small extent with increases in angle of attack (fig. 6(b)).

The gage drag coefficient C_{D_g} for the complete model with no internal flow appeared to have been noticeably affected by tunnel-boundary interference at a Mach number of 1.11 (fig. 12). The base-drag correction C_{D_b} applied to the gage drag coefficient C_{D_g} , however, corrected for much of the boundary interference (see C_D plot in fig. 12), since the measured base pressure coefficient P_b (fig. 7) also included the effects of boundary interference. The boundary-interference effects shown by the complete model with no internal flow were also shown but to a lesser extent by the fuselage alone with no internal flow (fig. 9).

Drag data at an angle of attack of 0° are shown in figure 21 for various configurations both with and without internal flow in the model. The drag data from the Langley tunnels showed satisfactory agreement for the fuselage alone with internal flow (fig. 21(a)). The agreement was generally poorer for the complete model with internal flow. Most of the differences in drag results for the complete model, however,

were probably within the accuracy of the measurements. The transonic drag rise of the model was 0.009 (fig. 21(a)). This small drag rise resulted from the high equivalent fineness ratio of the complete model, which was approximately 11, and the good approximation of the cross-sectional area distribution of the model to the optimum area distribution. With no internal flow in the model, the drag determinations made in the Langley tunnels showed good agreement (fig. 21(b)).

The speed brakes in both locations increased the drag coefficient C_{Dg} by approximately 0.07 at a lift coefficient of zero at transonic speeds (figs. 13(b), 16(b), and 17(b)), and the increase was greater at lifting conditions.

The roughness strip on the fuselage increased by a small amount the drag of the fuselage alone (fig. 8) and of the complete model (fig. 11).

Drag-Due-to-Lift Factor

The drag-due-to-lift factor $\Delta C_D / (\Delta C_L)^2$ shown in figure 22 is an average value applicable up to a lift coefficient of approximately 0.45. Also shown in figure 22 is the theoretical variation with Mach number of the drag-rise factor for zero leading-edge suction $1/57.3 \frac{dC_L}{d\alpha}$, where the derivative $dC_L/d\alpha$ was taken as the faired value of the experimental data on lift-curve slope shown in figure 18(a) for the complete model at a horizontal incidence of 0° .

The drag-due-to-lift factors obtained in the transonic tunnel tests were approximately 15 percent lower than those obtained in the high-speed tunnel tests. These differences were associated with the differences shown by the lift-curve slopes obtained in the two tunnels (fig. 18(a)).

Maximum Lift-Drag Ratio

The maximum lift-drag ratio of the complete model at two values of horizontal-tail incidence and of the complete model less horizontal tail is shown in figure 23 plotted against Mach number.

The values of maximum lift-drag ratio obtained in the Langley 8-foot-transonic-tunnel tests were higher than those obtained in the Langley high-speed 7- by 10-foot-tunnel tests as a result of the lower minimum drag coefficient and the lower drag-rise factor obtained in

the Langley 8-foot tunnel tests. The transonic tunnel results gave a maximum lift-drag ratio of 10.5 for the complete model less horizontal tail at a Mach number of 0.96. The results of an investigation on a wing-body combination with a comparable triangular wing of aspect ratio 3 and thickness ratio 0.03 and with no internal flow in the model gave a maximum lift-drag ratio of 13.5 at a Mach number of 0.92 (ref. 8). This latter configuration, however, was not a real airplane configuration.

The lift coefficient corresponding to maximum lift-drag ratio increased somewhat with Mach number at transonic speeds (fig. 24).

Effective Downwash

The effective downwash derivative $\Delta\epsilon/\Delta\alpha$ for the complete model is shown in figure 25. The effective downwash angle ϵ was obtained by using the horizontal-tail effectiveness $\Delta C_m/\Delta i_t$ presented in figure 20, and the slope $\Delta\epsilon/\Delta\alpha$ given in figure 25 is an average value for angles of attack from 0° to 4° .

The slope $\Delta\epsilon/\Delta\alpha$ decreased by approximately 20 percent at supersonic speeds. The agreement shown by the two tunnels was quite satisfactory.

Incremental Effect of Internal Flow

The incremental effect of internal flow on the aerodynamic coefficients at an angle of attack of 0° , as obtained from tests with and without the duct plug in the inlet, is shown in figure 26 for the fuselage alone and the complete model.

The inclusion of internal flow in the model by the removal of the duct plug from the fuselage alone and from the complete model resulted in a reduction in drag coefficient C_D by as much as 0.004 at transonic speeds, in a decrease in pitching-moment coefficient by essentially the same amount at all Mach numbers, and in only a generally small change in lift coefficient. The agreement shown by the data from the two tunnels was generally satisfactory.

Interference Effect of Mass-Flow Rake

The interference effect of the mass-flow rake on the flow over and in the model was generally small throughout the Mach number range at an angle of attack of 0° , as indicated by the lift, drag, and pitching-moment data of figure 10. The change in the interference effect on pitching-moment coefficient at Mach numbers of 1.04 and 1.10 may have

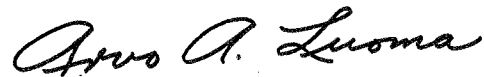
been associated with the tunnel-boundary interference effects present at these Mach numbers.

CONCLUSIONS

An investigation was made in the Langley 8-foot transonic tunnel of the longitudinal stability and control characteristics of a 1/30-scale model of the Republic XF-103 airplane. The effect of speed brakes located at the end of the fuselage was also investigated. Most of the tests were made with internal flow in the model but some data were obtained with no internal flow. The Reynolds number based on the mean aerodynamic chord of the wing was approximately 1.8×10^6 . The following conclusions are indicated:

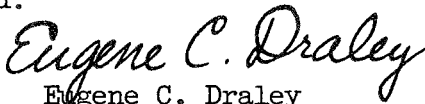
1. No serious longitudinal stability and control problems were evident at transonic speeds.
2. The transonic drag rise was small.
3. Speed brakes had no adverse effect on longitudinal stability.

Langley Aeronautical Laboratory,
National Advisory Committee for Aeronautics,
Langley Field, Va., August 11, 1954.



Arvo A. Luoma
Aeronautical Research Scientist

Approved:



Eugene C. Draley
Chief of Full-Scale Research Division

cg

REFERENCES

1. Lockwood, Vernard E., and Solomon, Martin: Stability and Control Characteristics at Low Speed of a 1/10-Scale Model of MX-1554A Design. NACA RM SL53A05, U. S. Air Force, 1953.
2. Smith, Willard G.: Wind-Tunnel Investigation of 1/15-Scale Model of Republic MX-1554 Airplane at Mach Numbers of 1.45 and 1.90. NACA RM SA53C17, 1953.
3. Dickey, Robert R., and Spahr, J. Richard: Wind-Tunnel Investigation of 1/60-Scale Model of MX-1554 Airplane at a Mach Number of 2.85. NACA RM SA53C18, 1953.
4. Lockwood, Vernard E., Luoma, Arvo A., and Solomon, Martin: Stability and Control Characteristics at High Subsonic Speeds of a 1/30-Scale Model of the MX-1554A Design. NACA RM SL53K12a, 1953.
5. Wright, Ray H., and Ward, Vernon G.: NACA Transonic Wind-Tunnel Test Sections. NACA RM L8J06, 1948.
6. Ritchie, Virgil S., and Pearson, Albin O.: Calibration of the Slotted Test Section of the Langley 8-Foot Transonic Tunnel and Preliminary Experimental Investigation of Boundary-Reflected Disturbances. NACA RM L51K14, 1952.
7. Wright, Ray H., and Ritchie, Virgil S.: Characteristics of a Transonic Test Section With Various Slot Shapes in the Langley 8-Foot High-Speed Tunnel. NACA RM L51H10, 1951.
8. Hall, Charles F.: Lift, Drag, and Pitching Moment of Low-Aspect-Ratio Wings at Subsonic and Supersonic Speeds. NACA RM A53A30, 1953.

TABLE I.- CONFIGURATIONS, TEST CONDITIONS, AND INDEX OF BASIC FIGURES

Configuration	Model condition	α , deg	i_t , deg	M	Mass-flow rake	Internal flow in model	Figure
Fuselage alone	Both smooth and transition strip on fuselage	0	---	0.60 to 1.15	Off	Yes	8
Fuselage alone plus duct plug	Smooth	0	---	0.40 to 1.14	Off	No	9
Complete model	Smooth	0	0	0.40 to 1.15	Both off and on	Yes	10
Complete model	Both smooth and transition strip on fuselage	0	0	0.40 to 1.15	Off	Yes	11
Complete model plus duct plug	Smooth	0	0	0.40 to 1.15	Off	No	12
Complete model	Smooth	-2 to 15 (approx.)	0	0.90, 0.96, 0.98, 1.02, and 1.13	On at $M_0 = 0.96$ and off at other M_0 's	Yes	13
Complete model	Smooth	-2 to 15 (approx.)	-5	0.96, 0.98, 1.02, and 1.13	Off	Yes	14
Complete model less horizontal tail	Smooth	-2 to 15 (approx.)	---	0.96, 0.98, 1.02, and 1.12	On	Yes	15
Complete model plus speed brakes in location 1	Smooth	-1 to 16 (approx.)	0	0.90, 0.96, 1.02, and 1.13	Off	Yes	16
Complete model plus speed brakes in location 2	Smooth	-2 to 15 (approx.)	0	0.90, 0.96, 1.02, and 1.13	Off	Yes	17

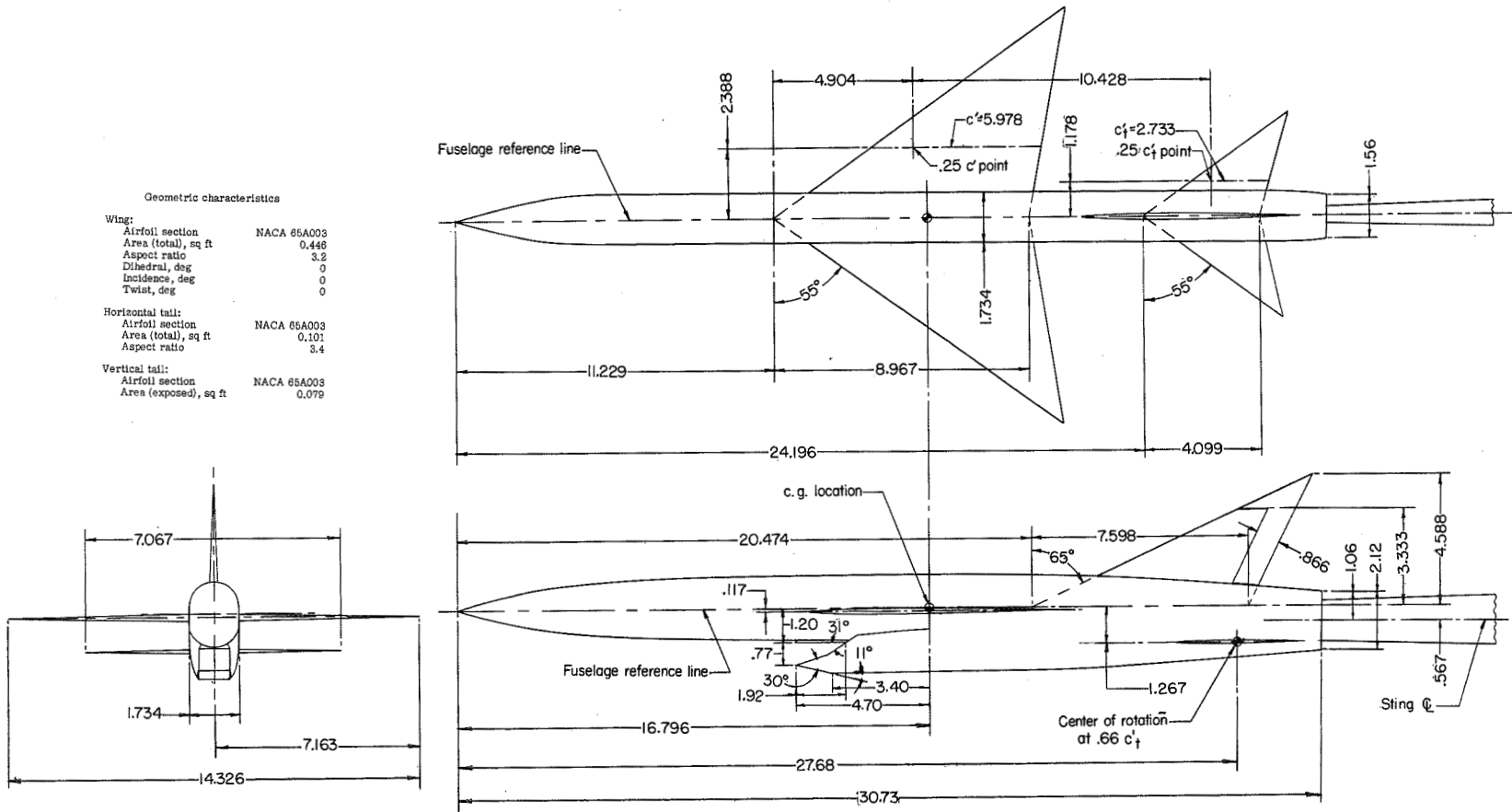
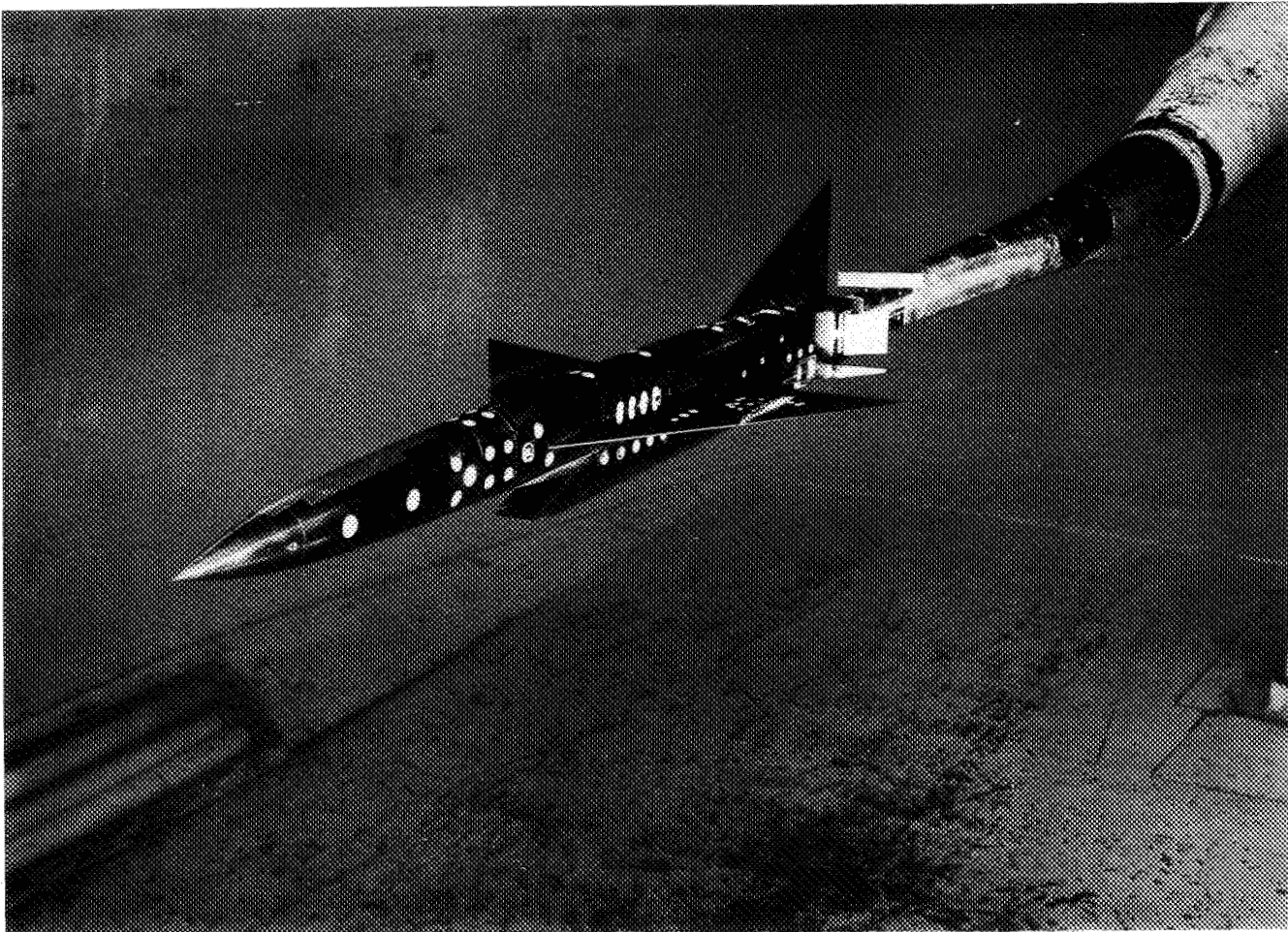
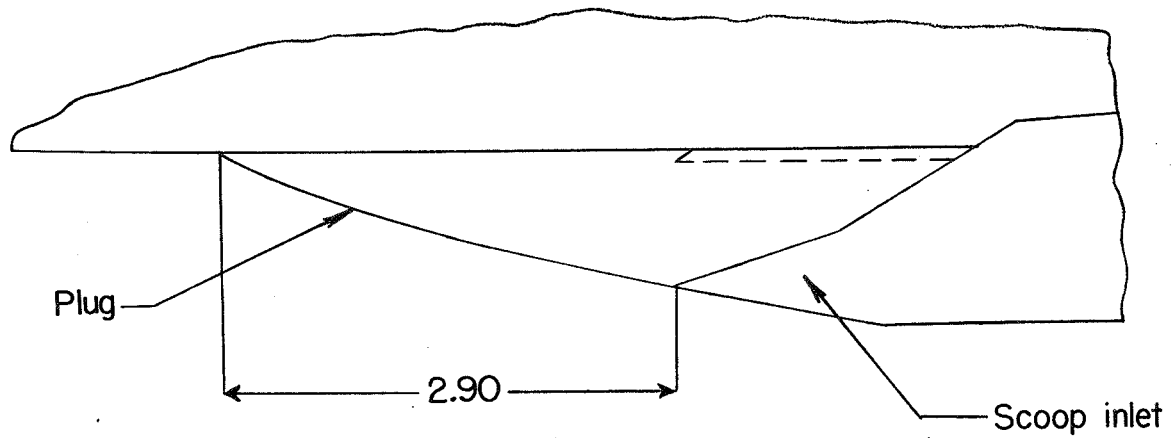


Figure 1.- General arrangement of 1/22-scale model of Republic XF-103 airplane as tested in Langley 8-foot transonic tunnel. (All dimensions in inches except as noted.)

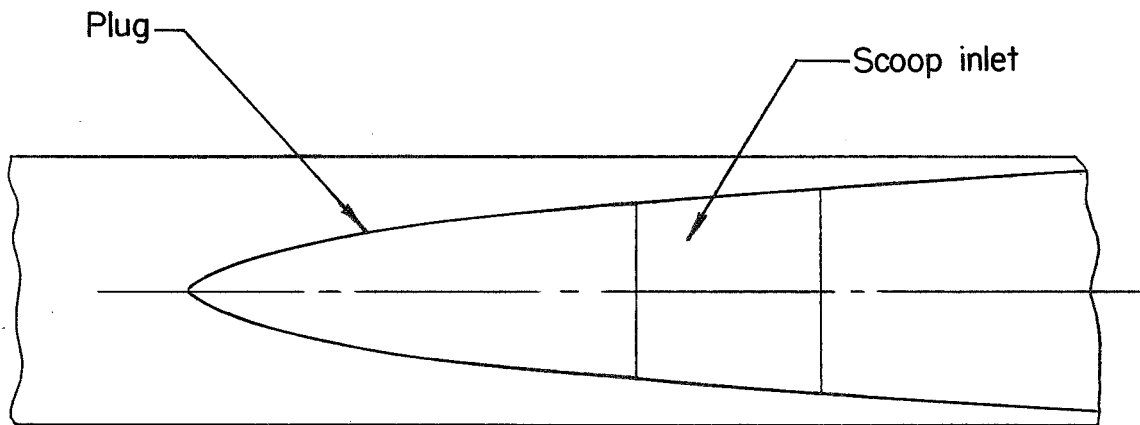


L-79965.1

Figure 2.- Installation of 1/30-scale model of Republic XF-103 airplane in Langley high-speed 7- by 10-foot tunnel. Complete model plus wing fences plus 45° speed brakes in location 1.



Side view



Bottom view

Figure 3.- Outline of plug for duct inlet. (All dimensions in inches.)

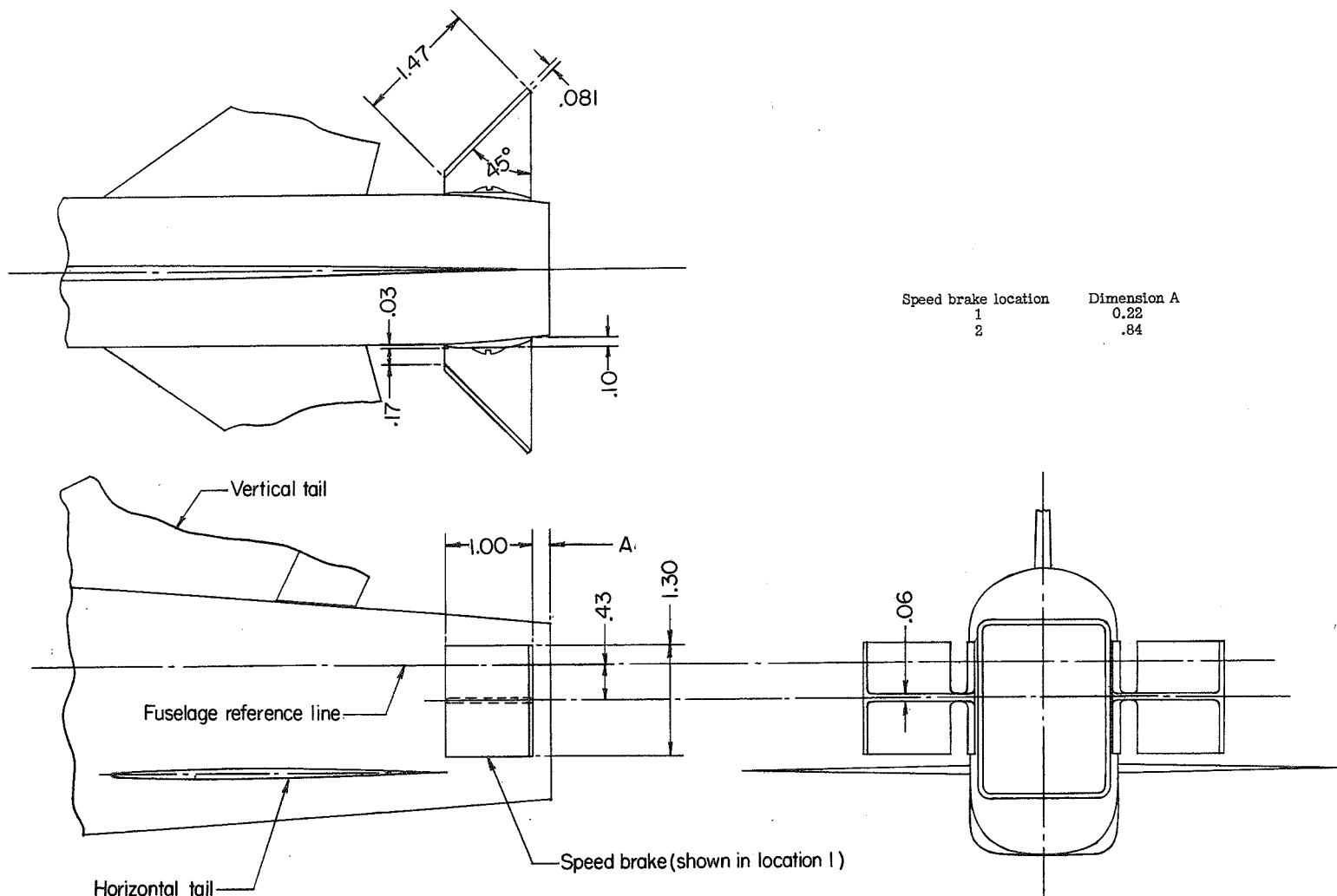


Figure 4.- Dimensions of 45° speed brake and location on fuselage. (All dimensions in inches except as noted.)

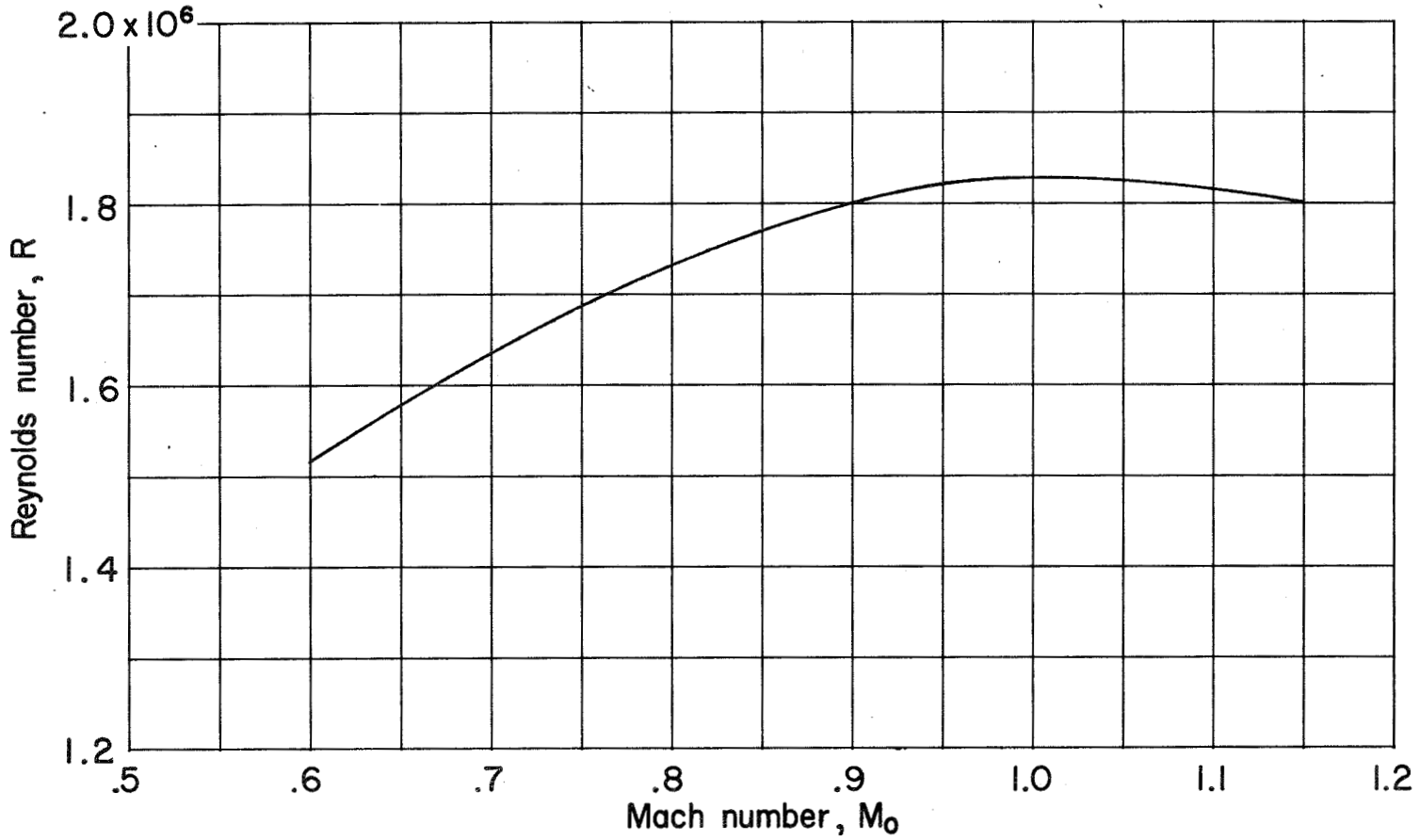
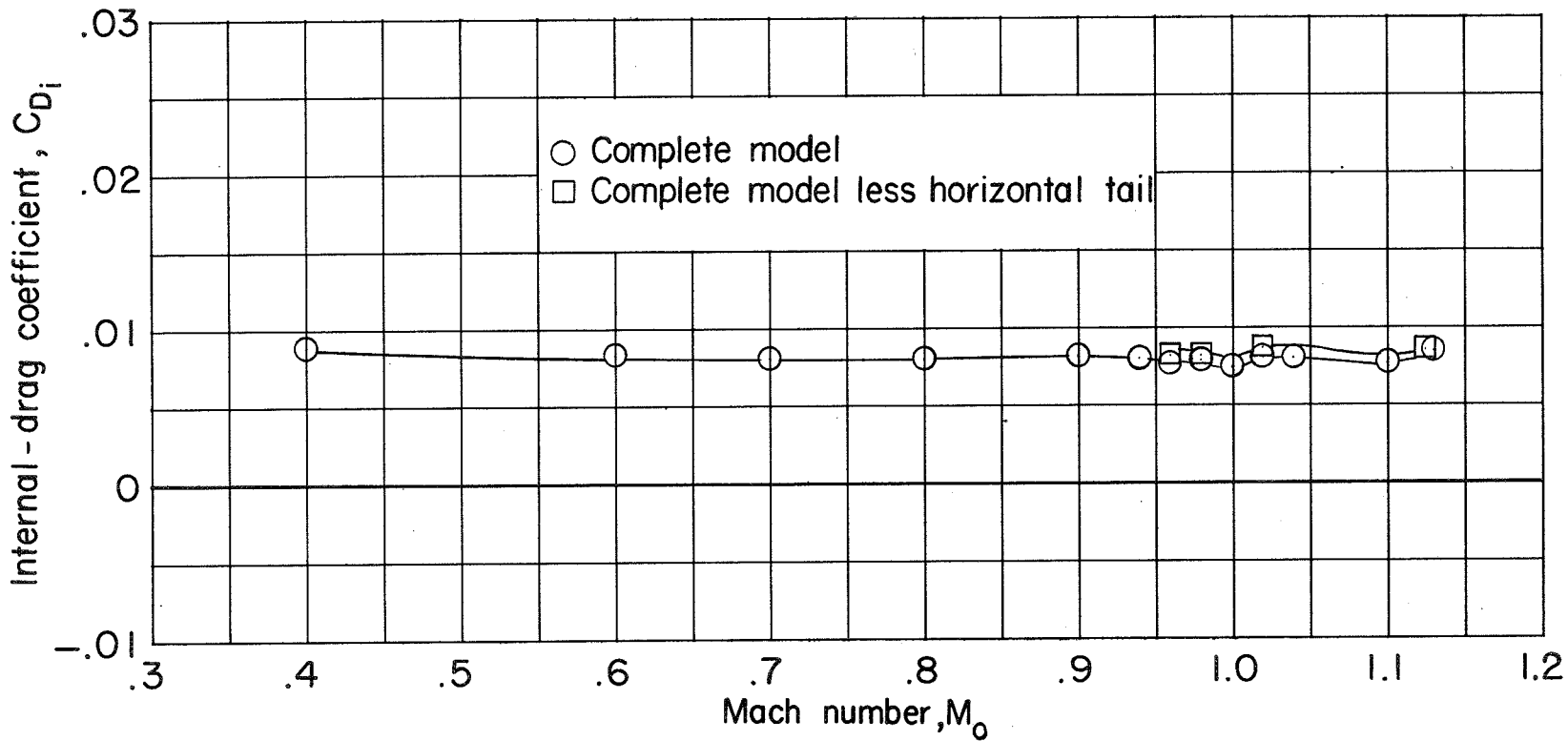
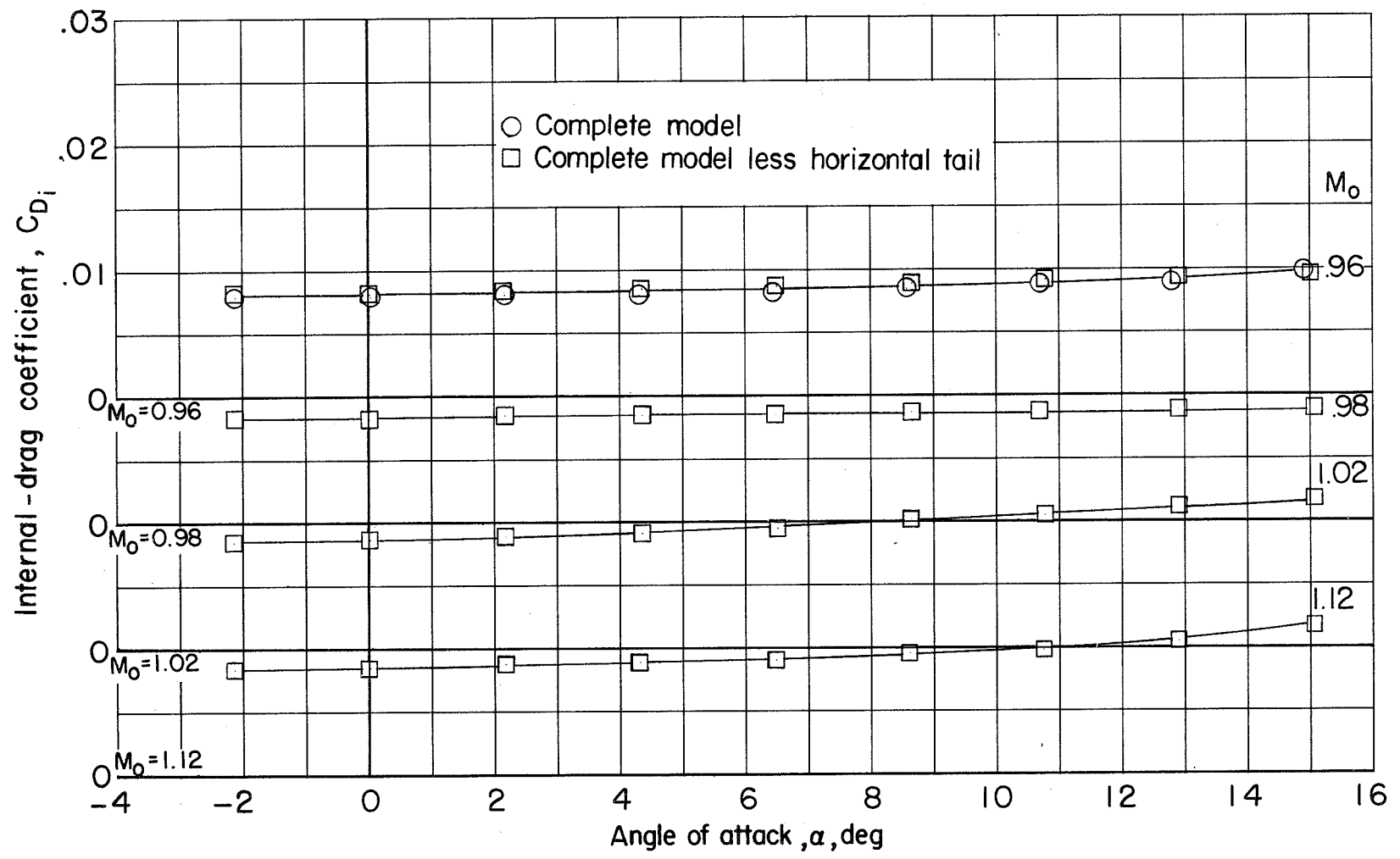


Figure 5.- Variation of average Reynolds number (based on mean aerodynamic chord of wing) with Mach number in tests of 1/30-scale model of Republic XF-103 airplane in Langley 8-foot transonic tunnel.



(a) Variation with Mach number; $\alpha = 0^\circ$.

Figure 6.- Variation of internal drag coefficient with Mach number and angle of attack.



(b) Variation with angle of attack.

Figure 6.- Concluded.

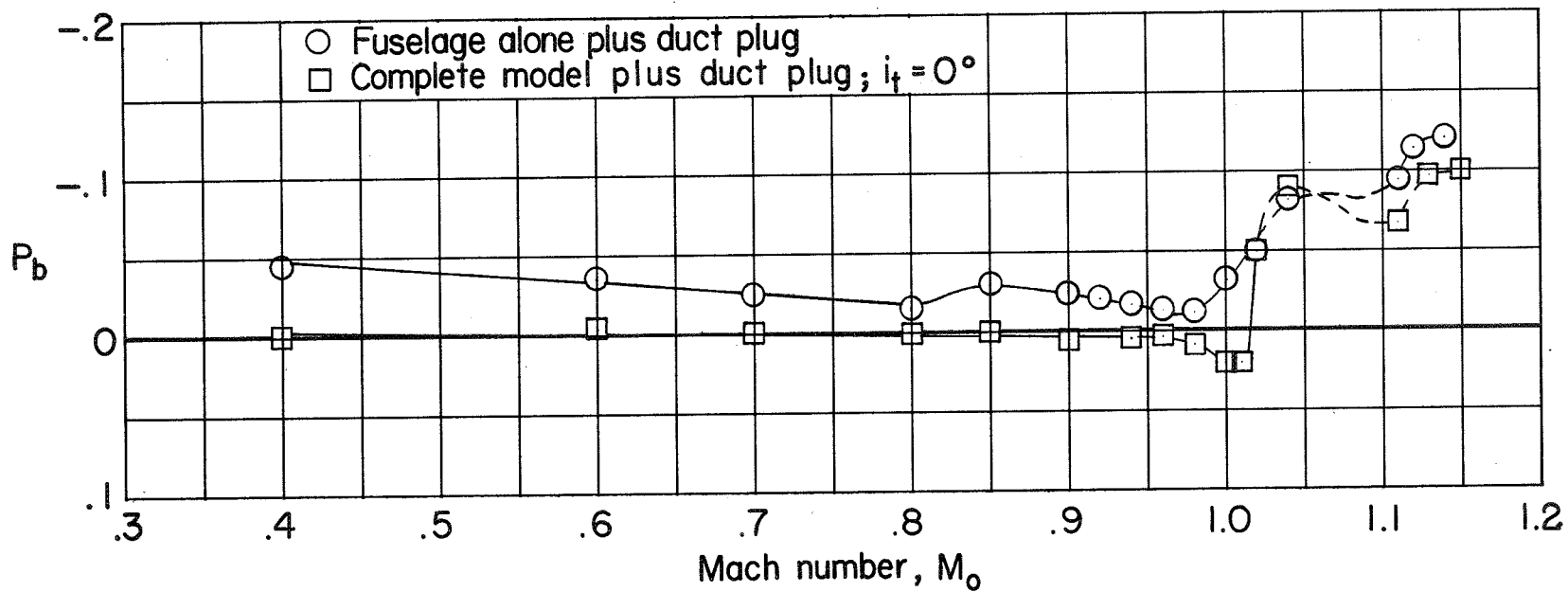


Figure 7.- Variation of base-pressure coefficient with Mach number.
 $\alpha = 0^\circ$. No internal flow in model. Mass-flow rake off.

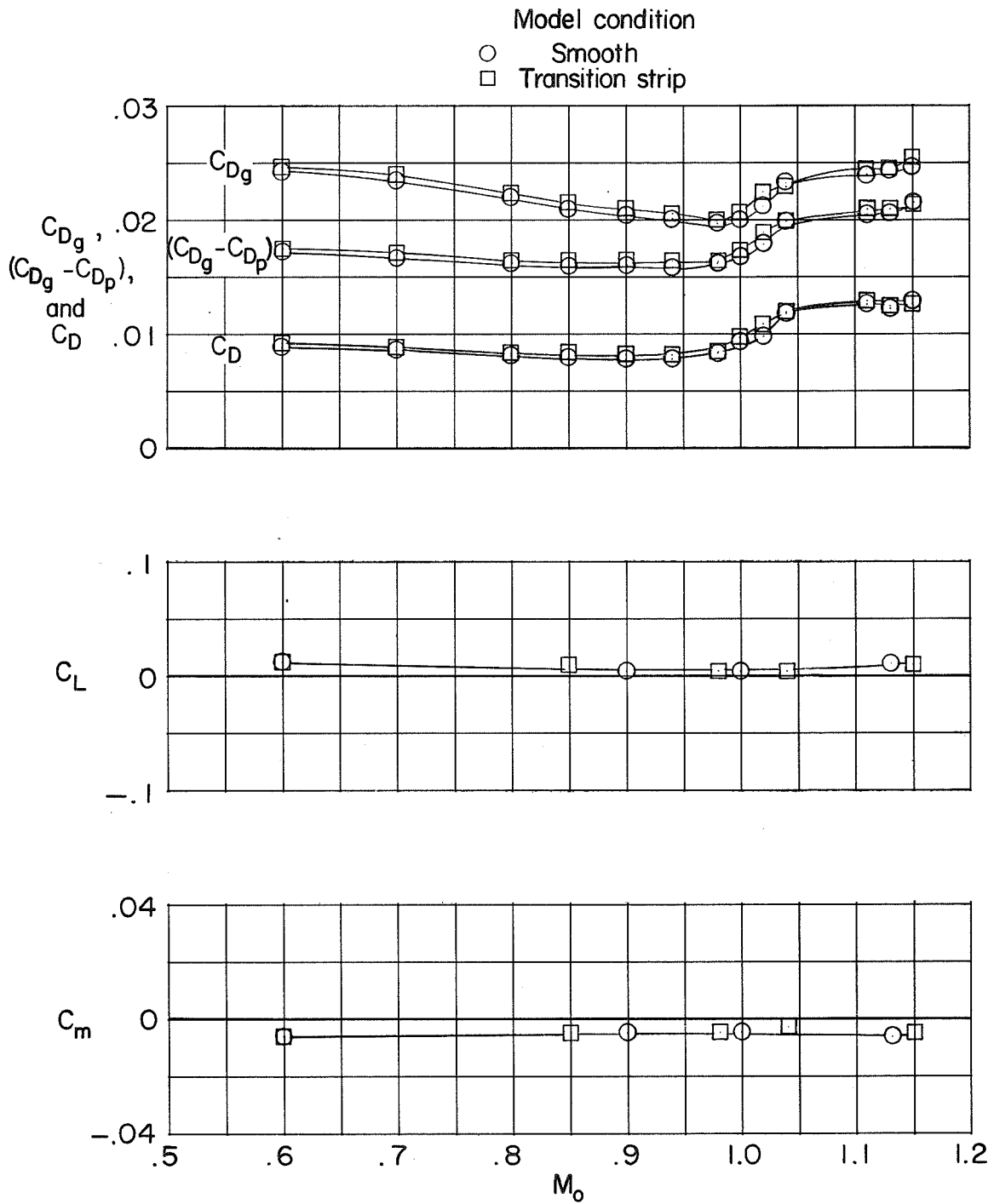


Figure 8.- Variation of aerodynamic characteristics with Mach number. Fuselage alone; $\alpha = 0^\circ$. Internal flow in model. Mass-flow rake off.

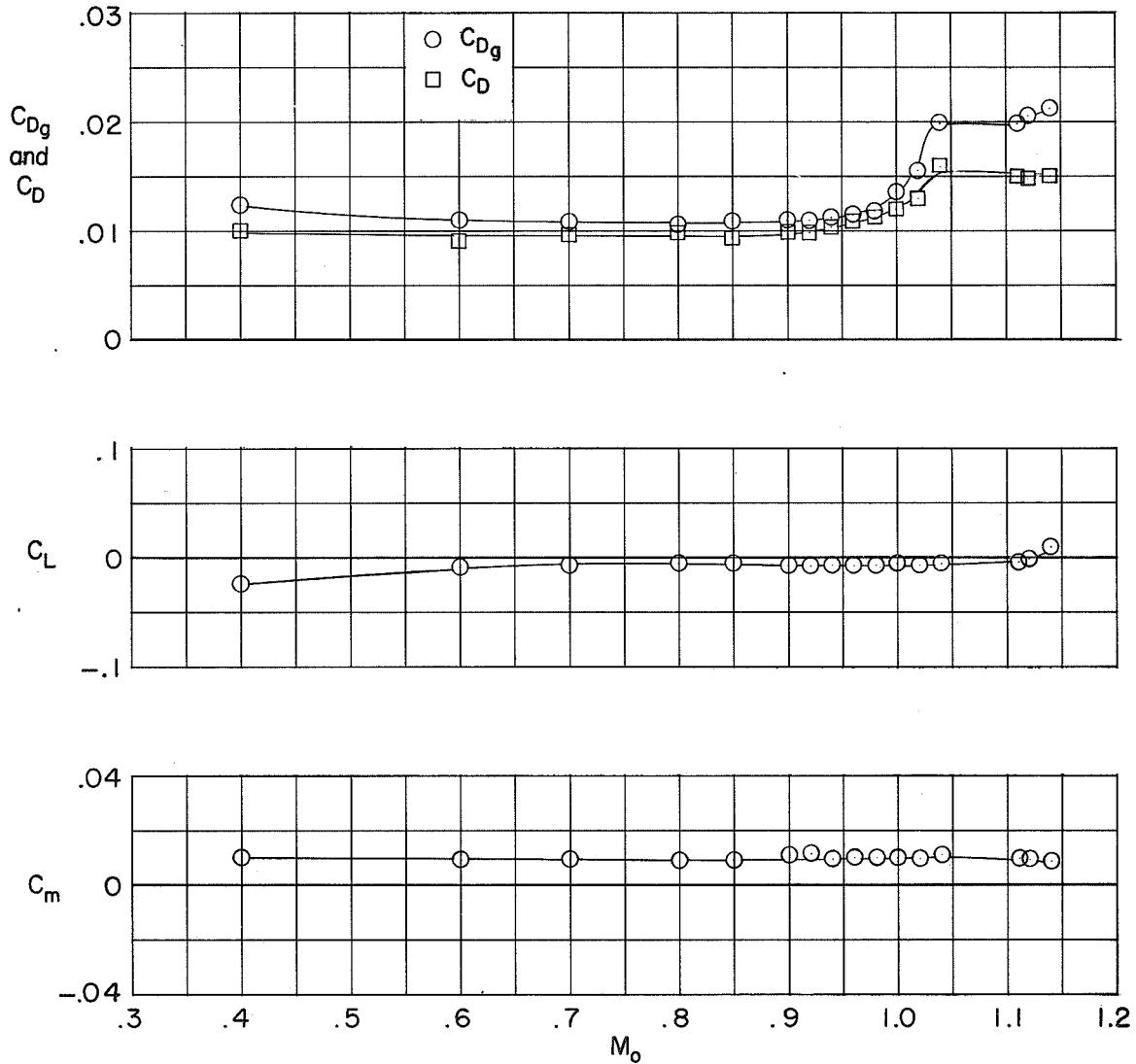


Figure 9.- Variation of aerodynamic characteristics with Mach number. Fuselage alone plus duct plug; $\alpha = 0^\circ$; no internal flow in model; mass-flow rake off.

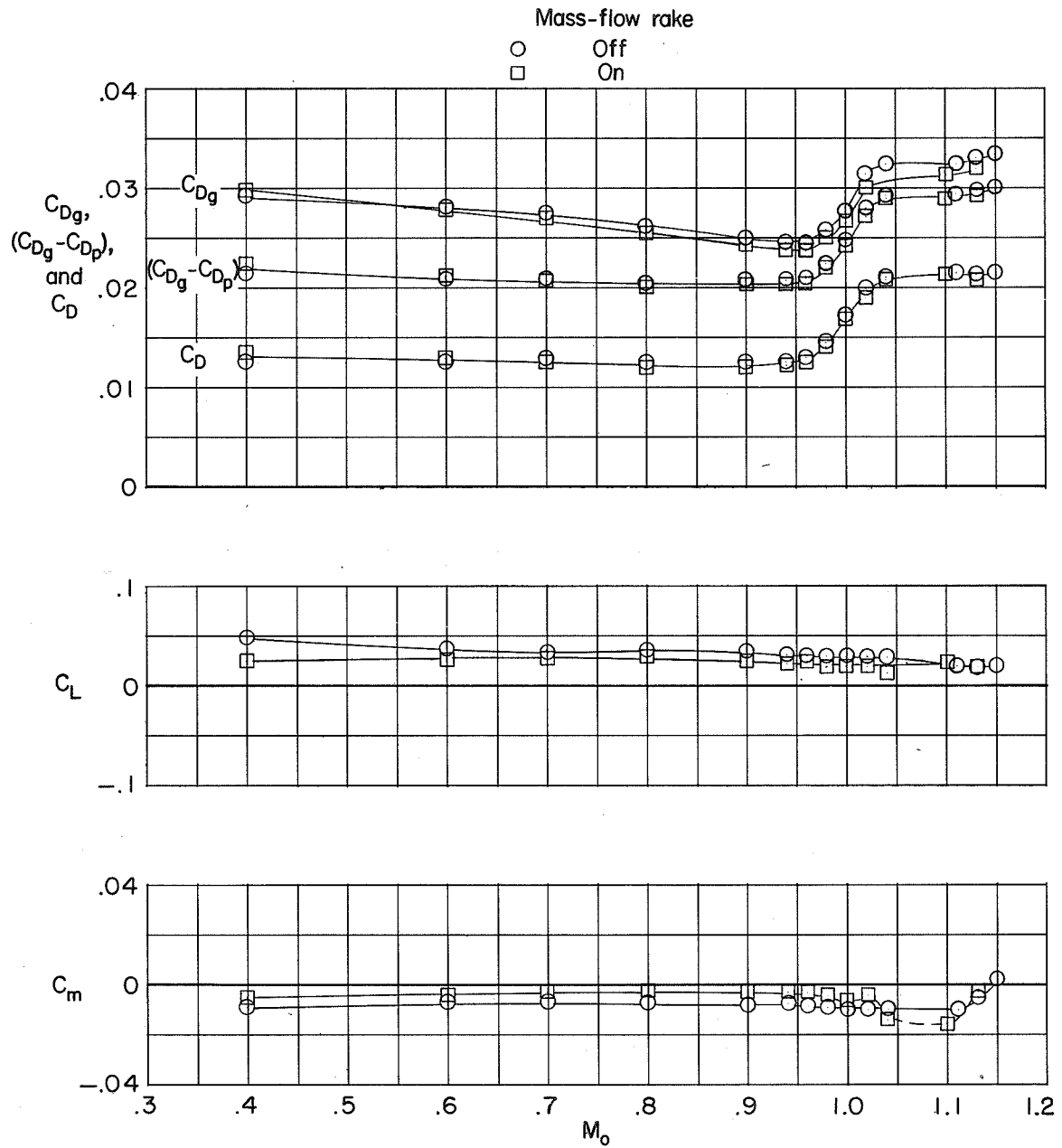


Figure 10.- Variation of aerodynamic characteristics with Mach number. Complete model; $i_t = 0^\circ$; $\alpha = 0^\circ$; internal flow in model; mass-flow rake both off and on.

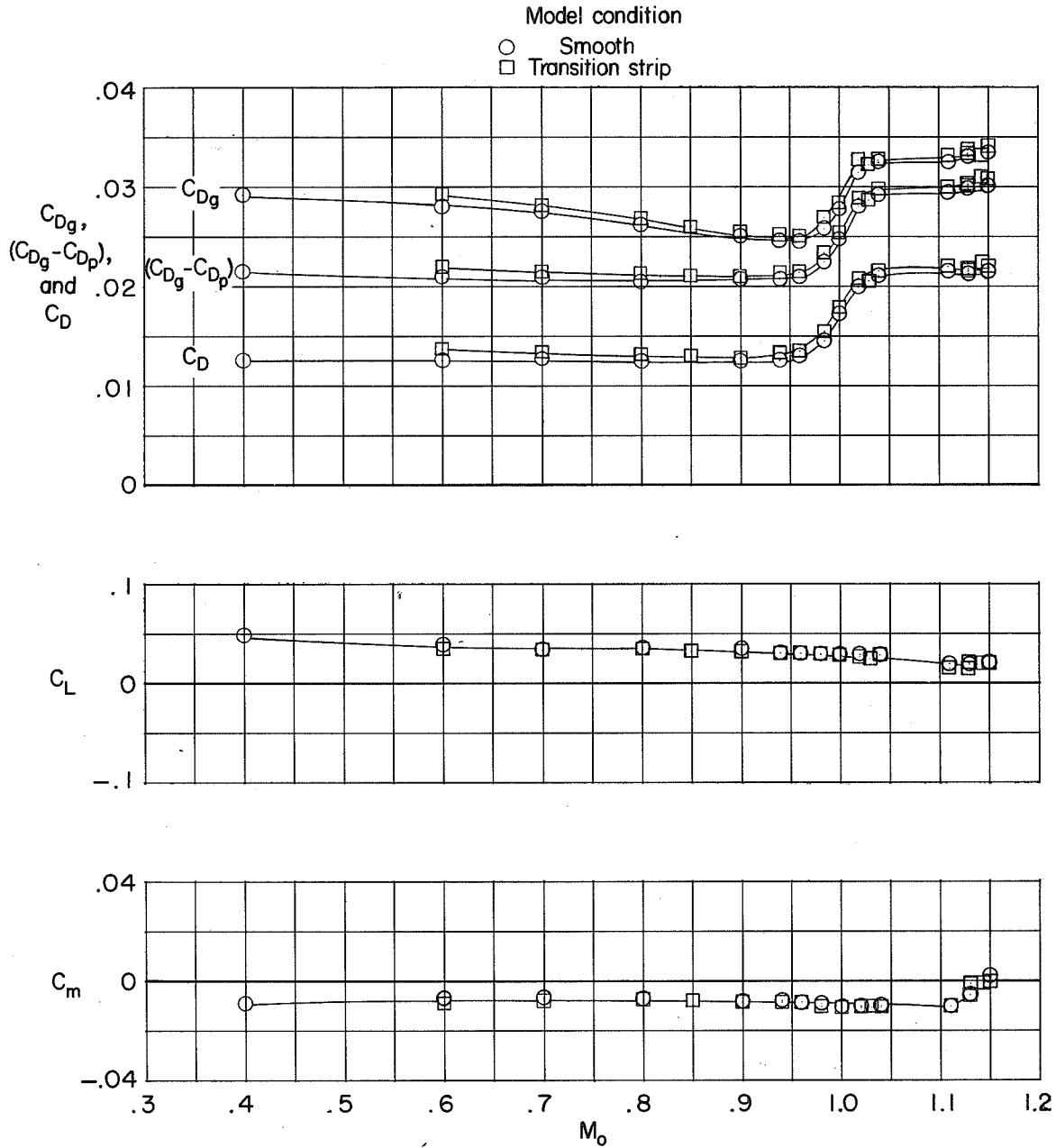


Figure 11.- Effect of transition strip on aerodynamic characteristics. Complete model; $i_t = 0^\circ$; $\alpha = 0^\circ$; internal flow in model; mass-flow rake off.

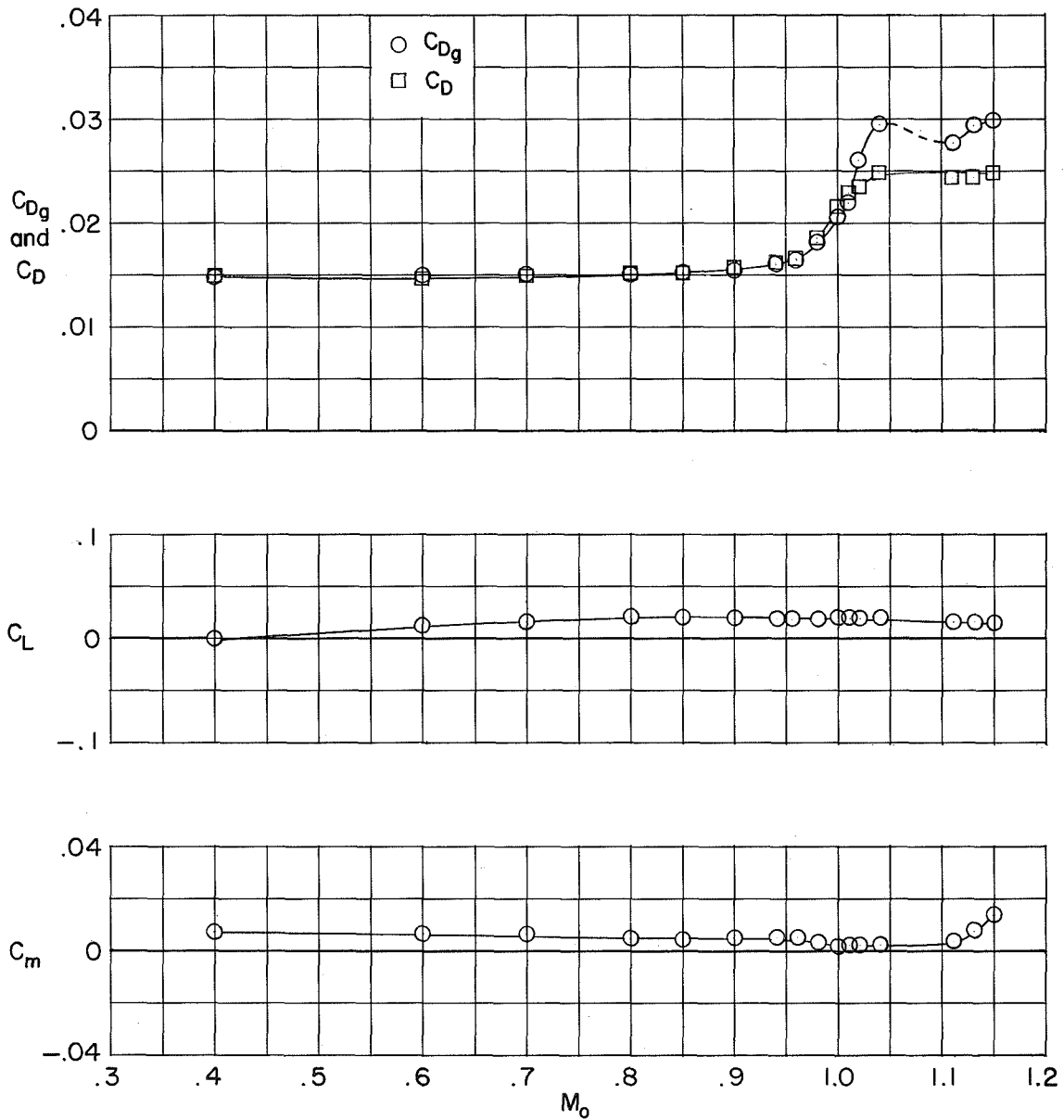
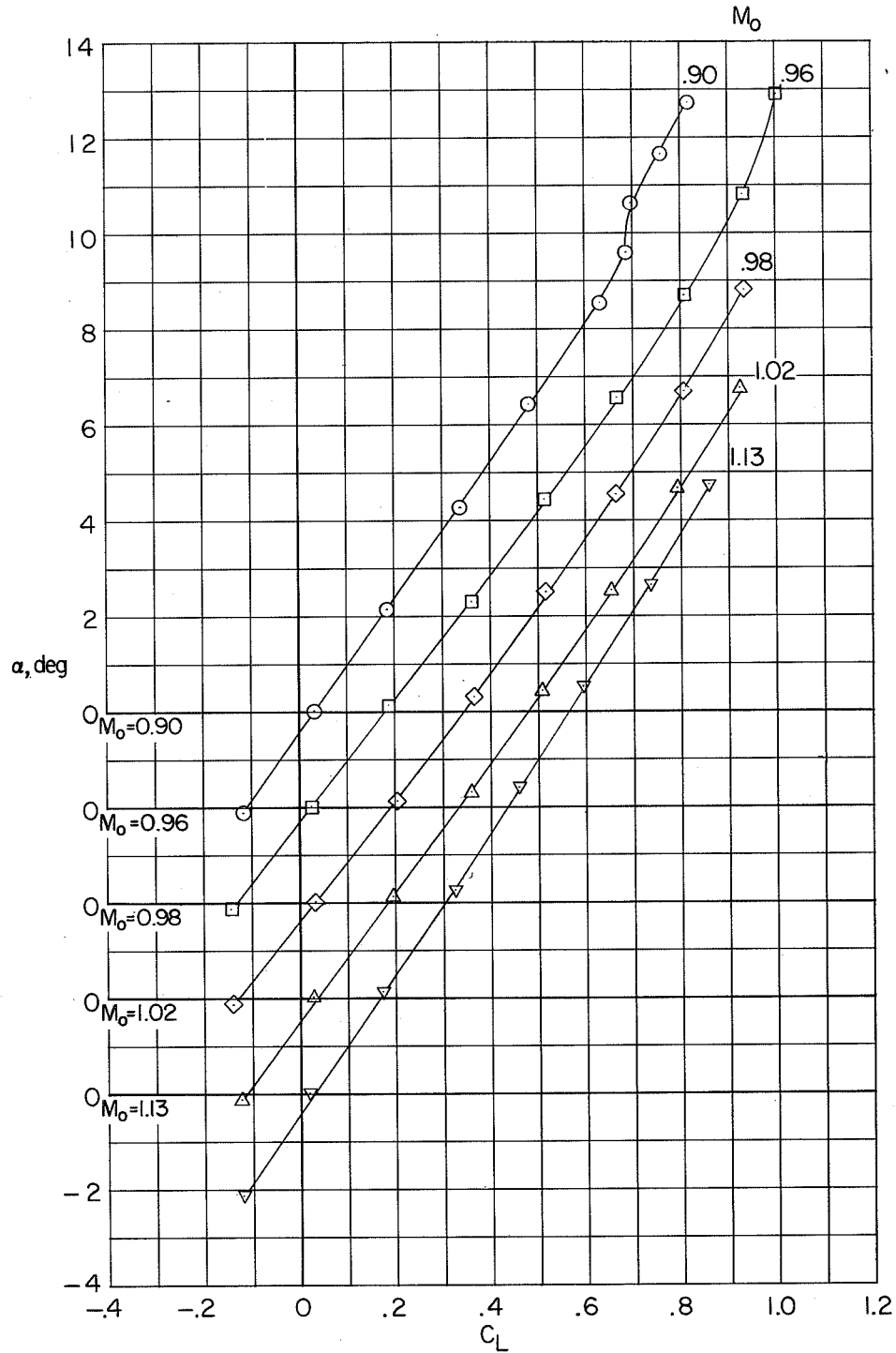
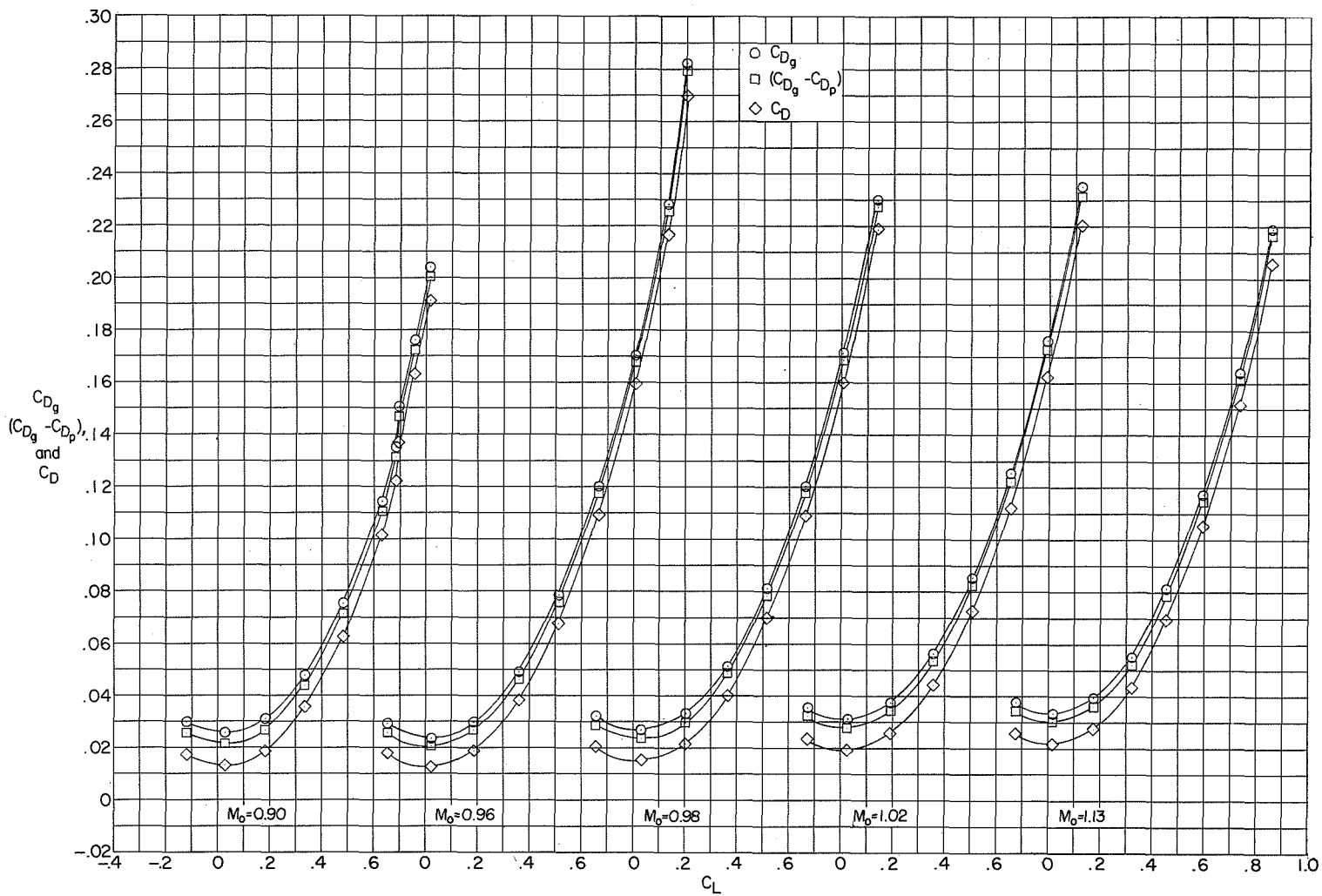


Figure 12.- Variation of aerodynamic characteristics with Mach number. Complete model plus duct plug; $i_t = 0^\circ$; $\alpha = 0^\circ$; no internal flow in model; mass-flow rake off.



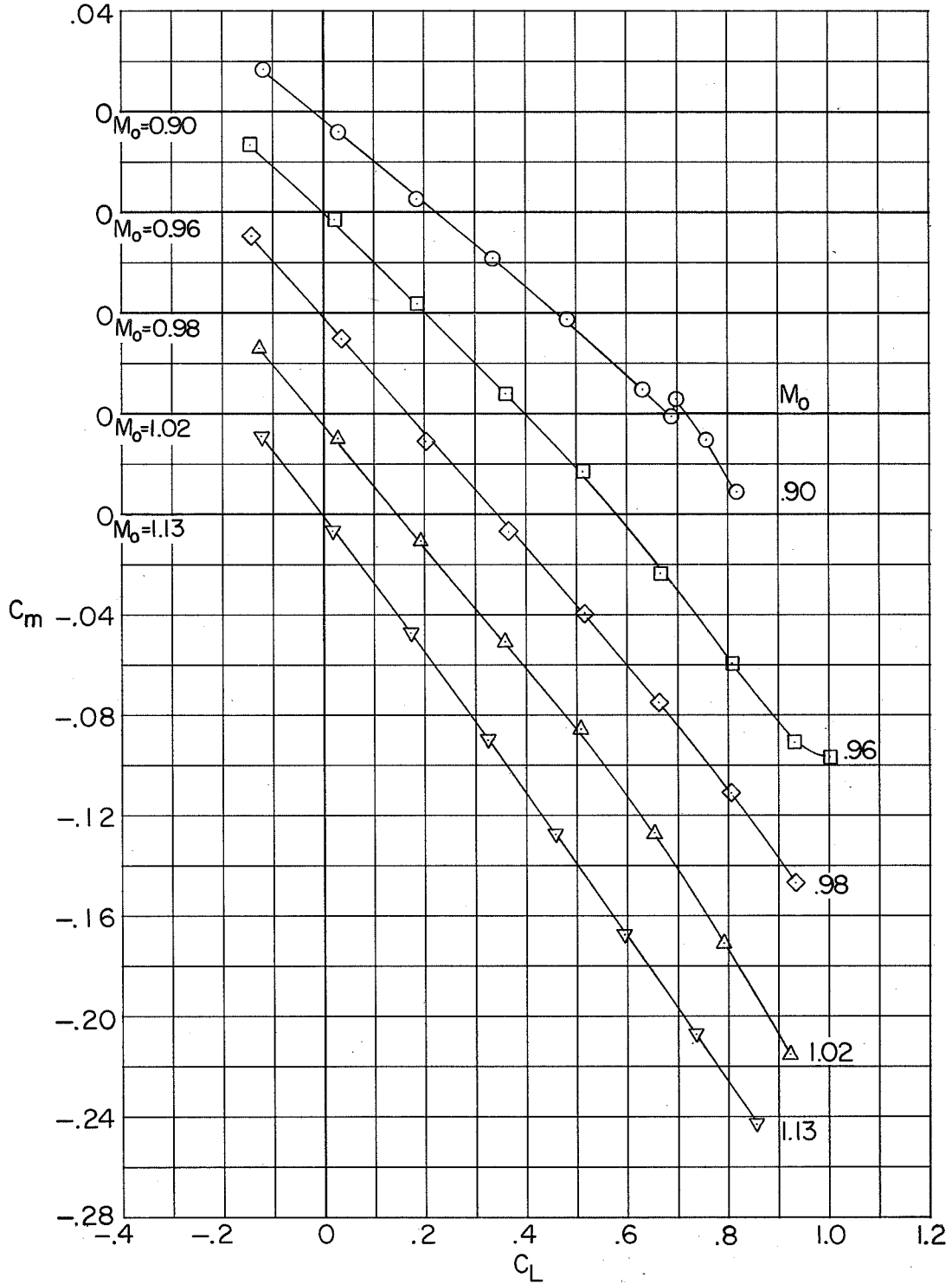
(a) Angle of attack.

Figure 13.- Variation of aerodynamic coefficients with lift coefficient. Complete model; $i_t = 0^\circ$; internal flow in model; mass-flow rake on at Mach number of 0.96 and off at other Mach numbers.



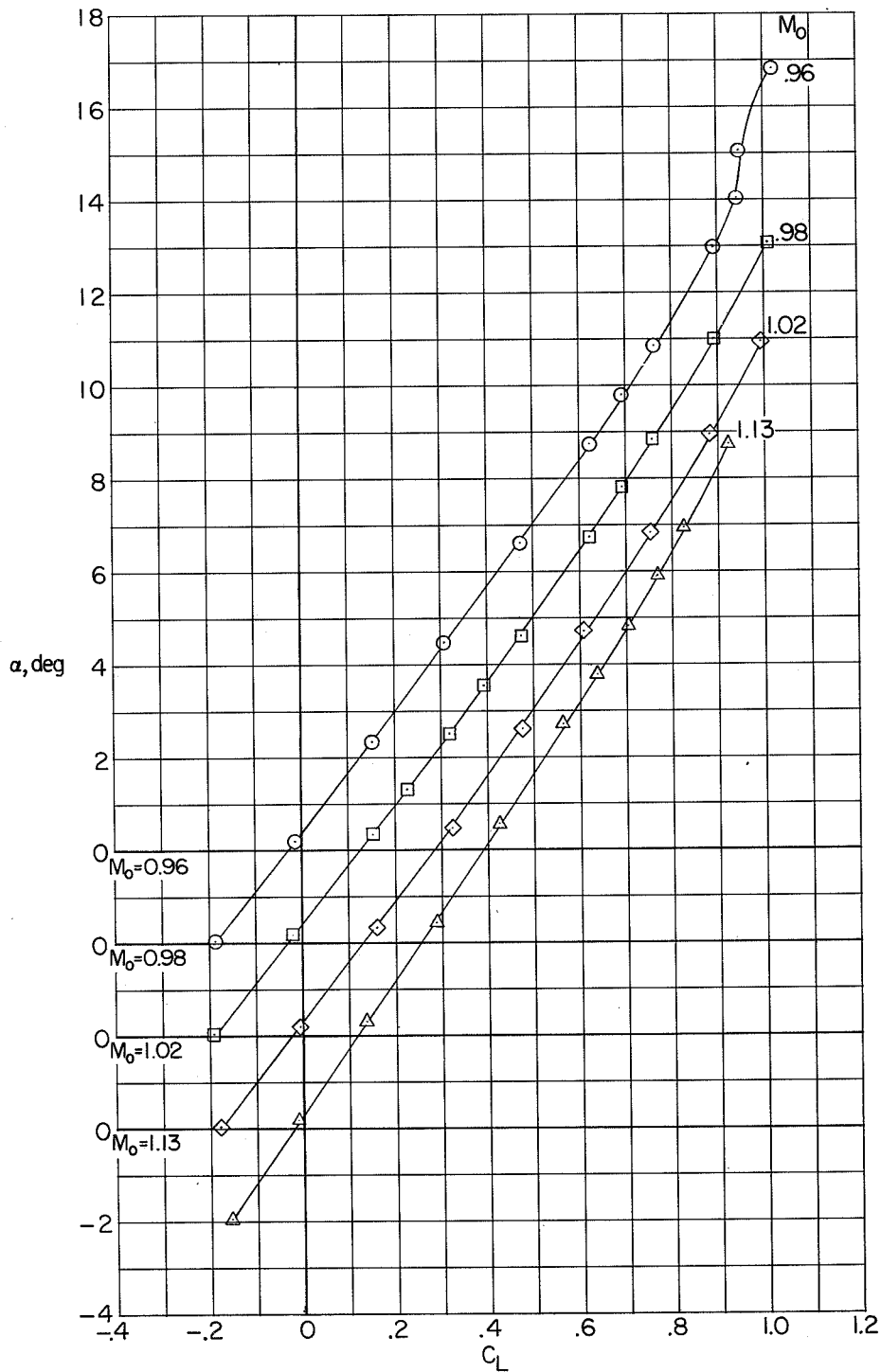
(b) Drag coefficient.

Figure 13.- Continued.



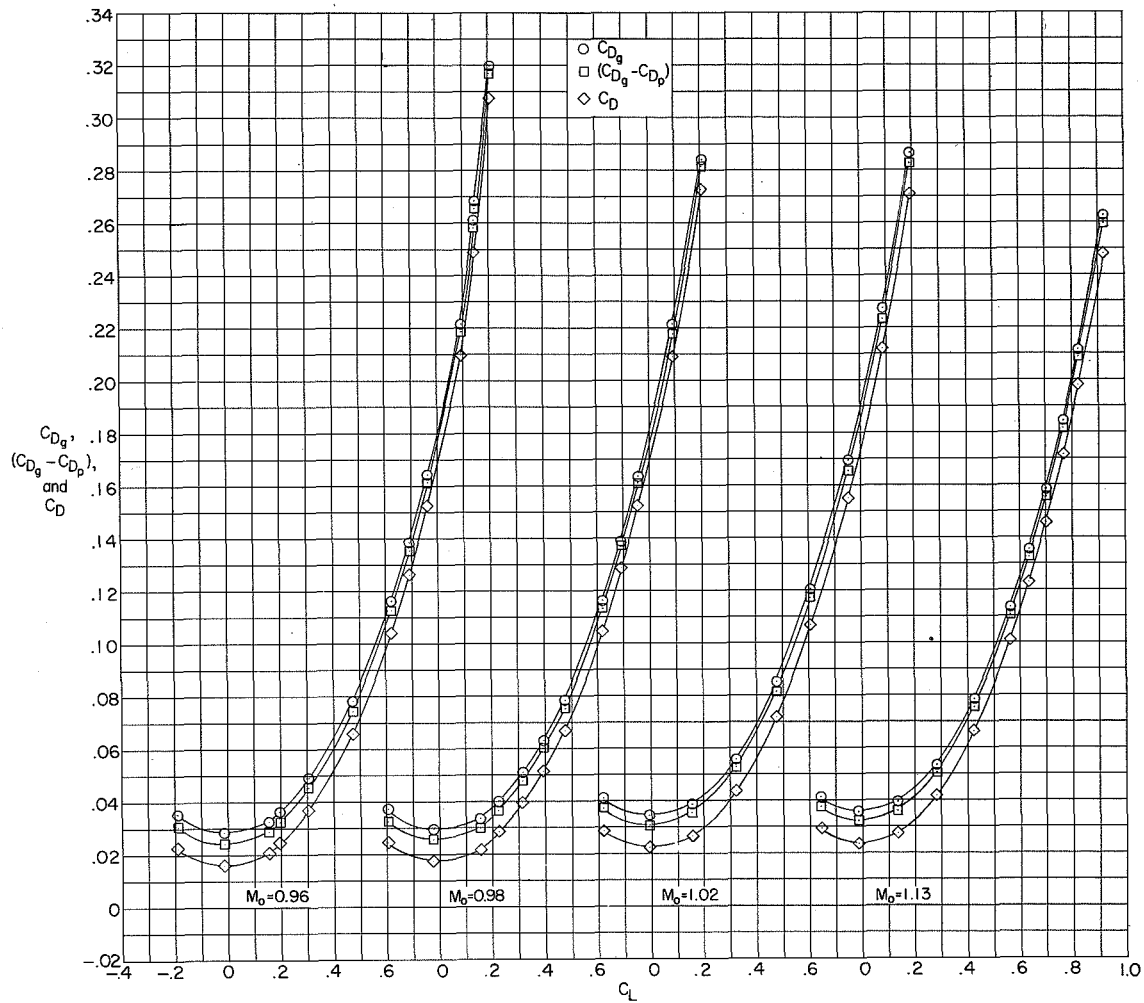
(c) Pitching-moment coefficient.

Figure 13.- Concluded.



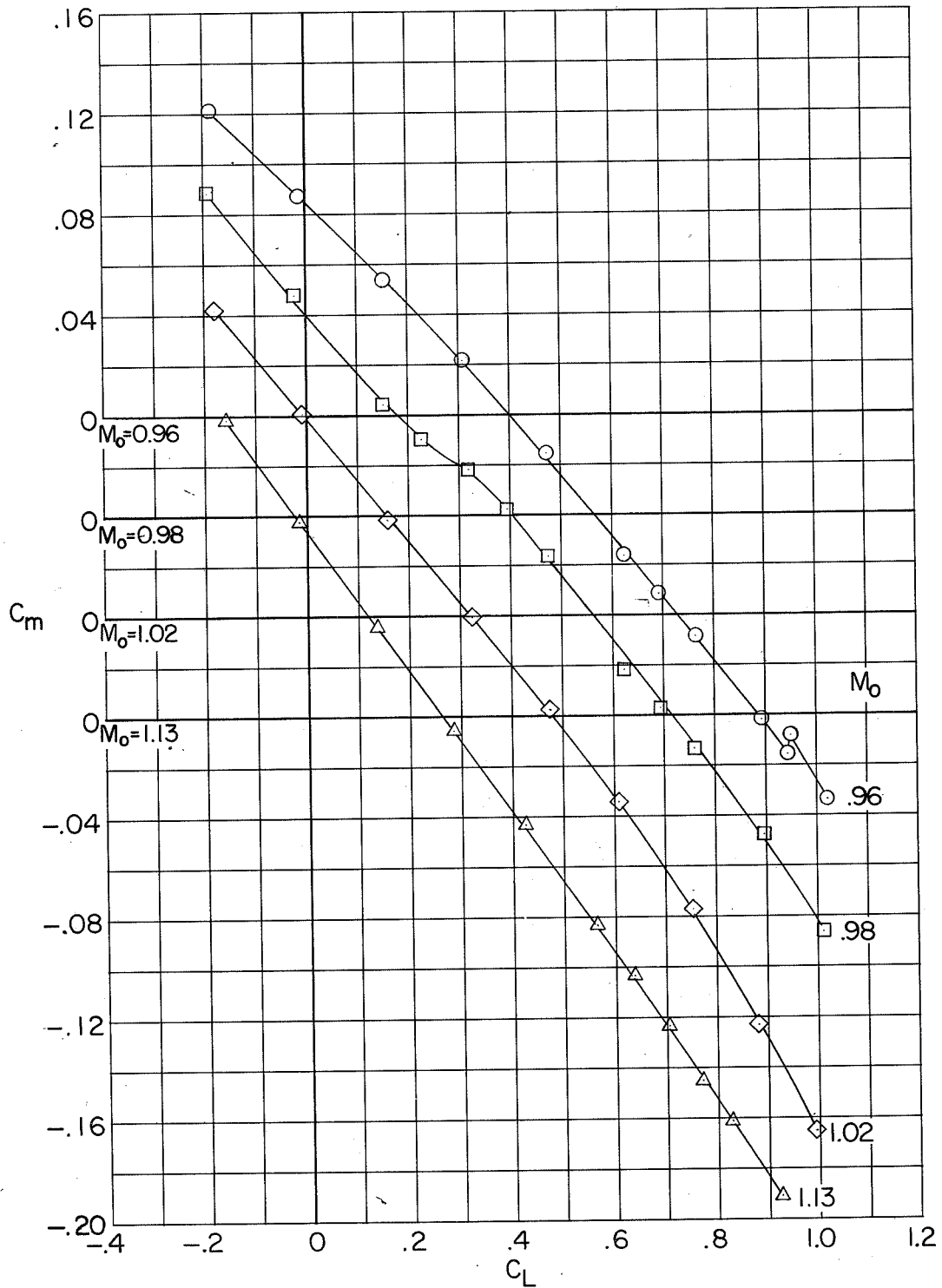
(a) Angle of attack.

Figure 14.- Variation of aerodynamic coefficients with lift coefficient. Complete model; $i_t = -5^\circ$; internal flow in model; mass-flow rake off.



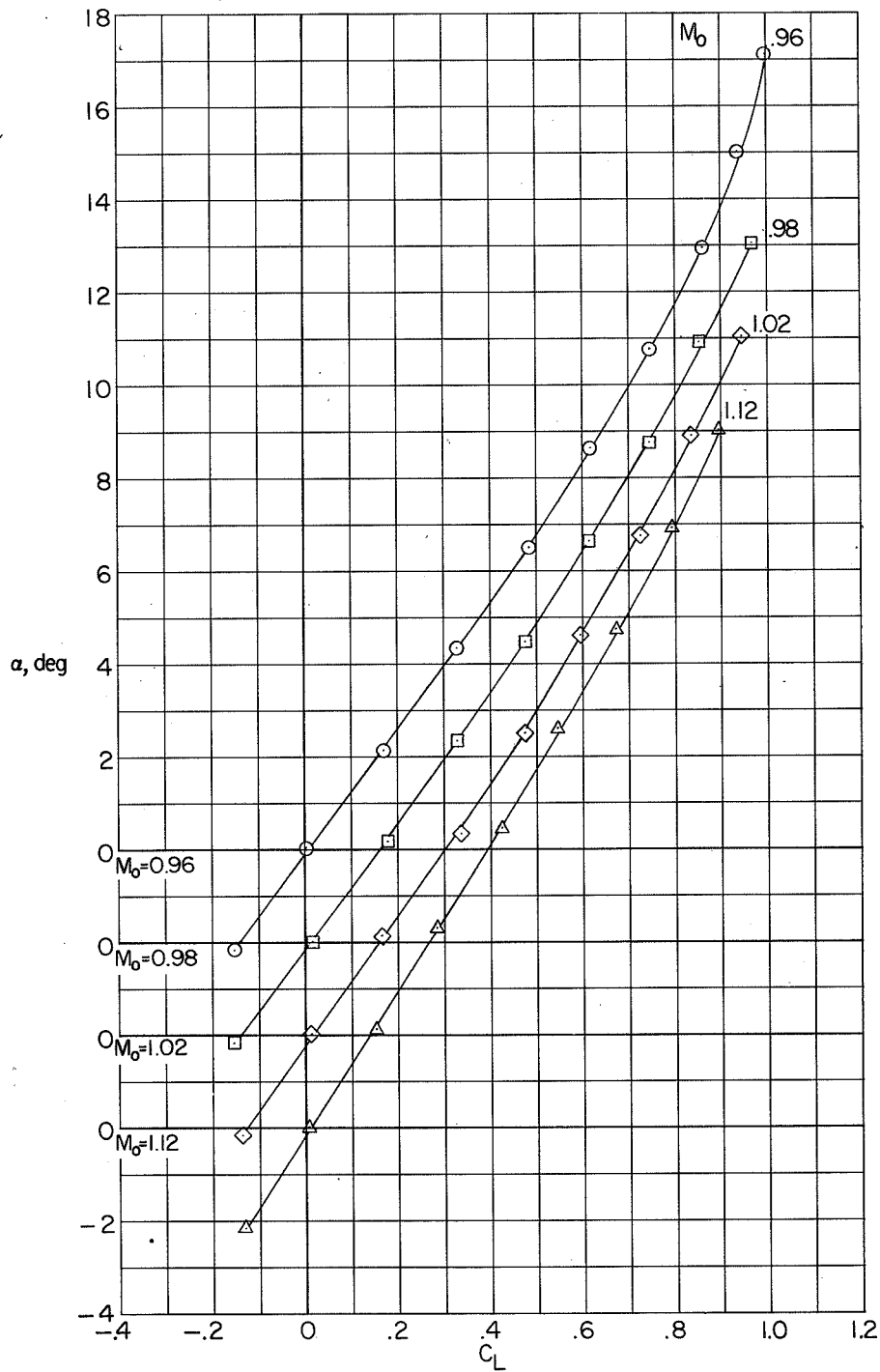
(b) Drag coefficient.

Figure 14.- Continued.



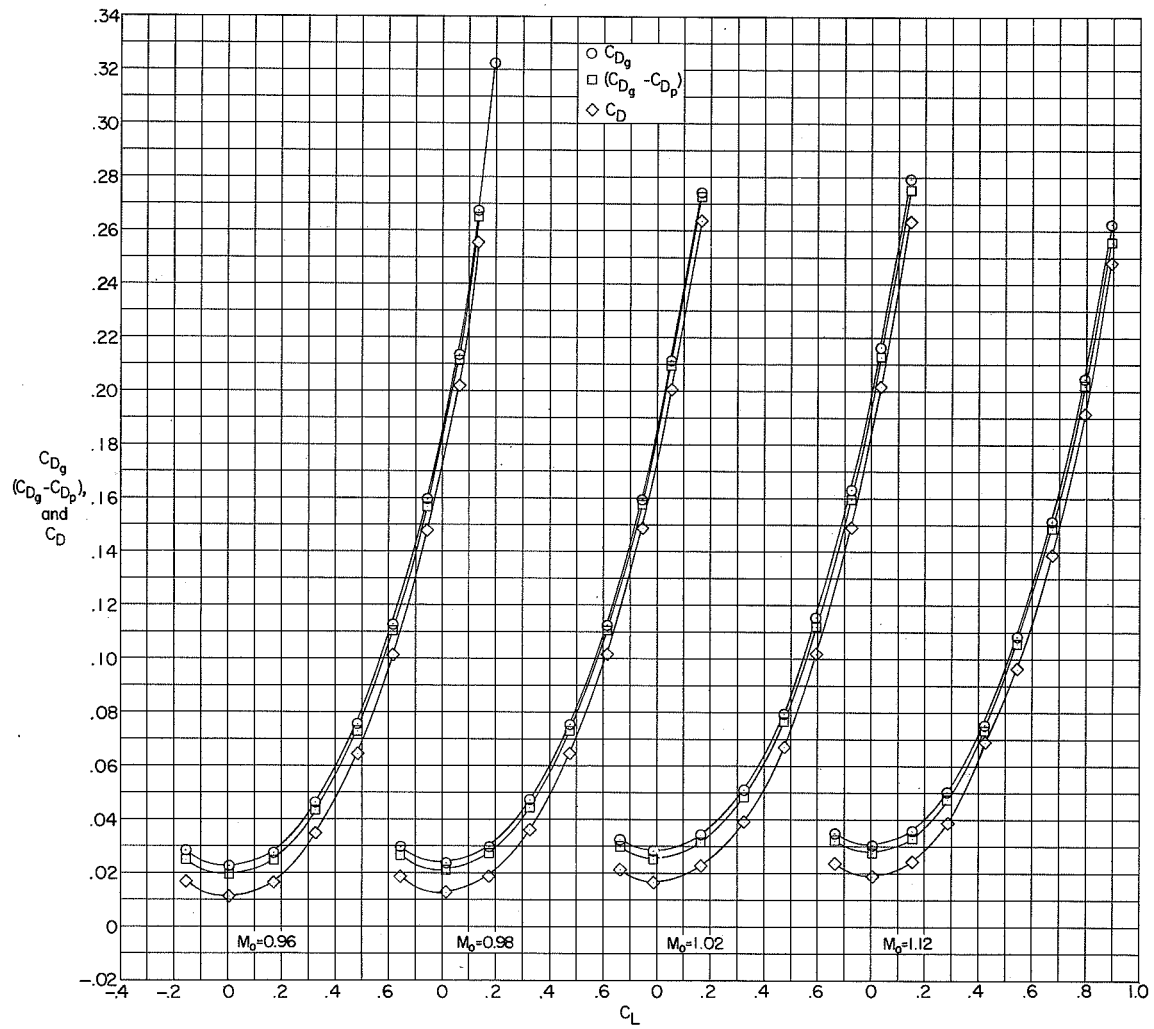
(c) Pitching-moment coefficient.

Figure 14.- Concluded.



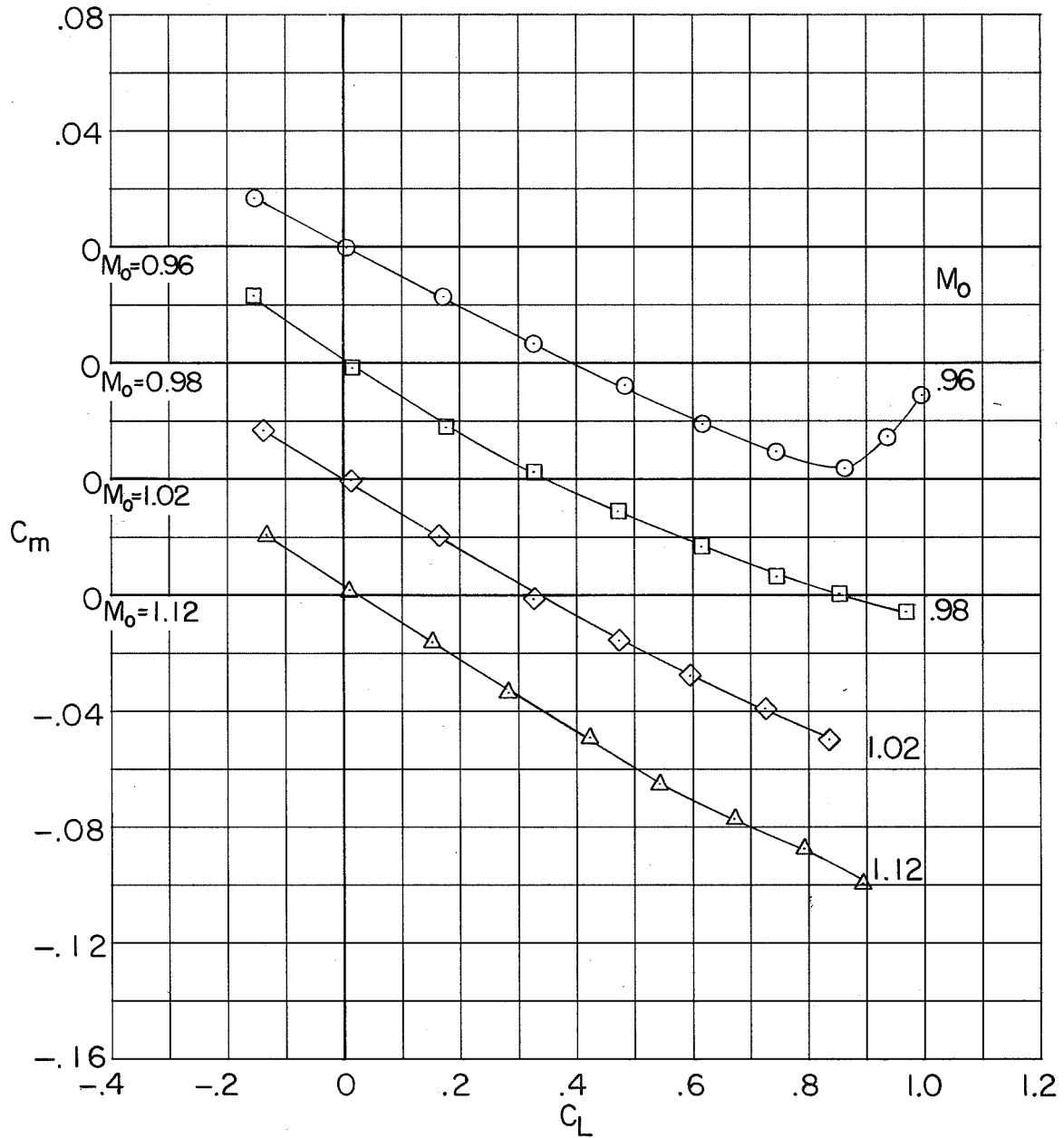
(a) Angle of attack.

Figure 15.- Variation of aerodynamic coefficients with lift coefficient.
 Complete model less horizontal tail; internal flow in model; mass-flow
 rake on.



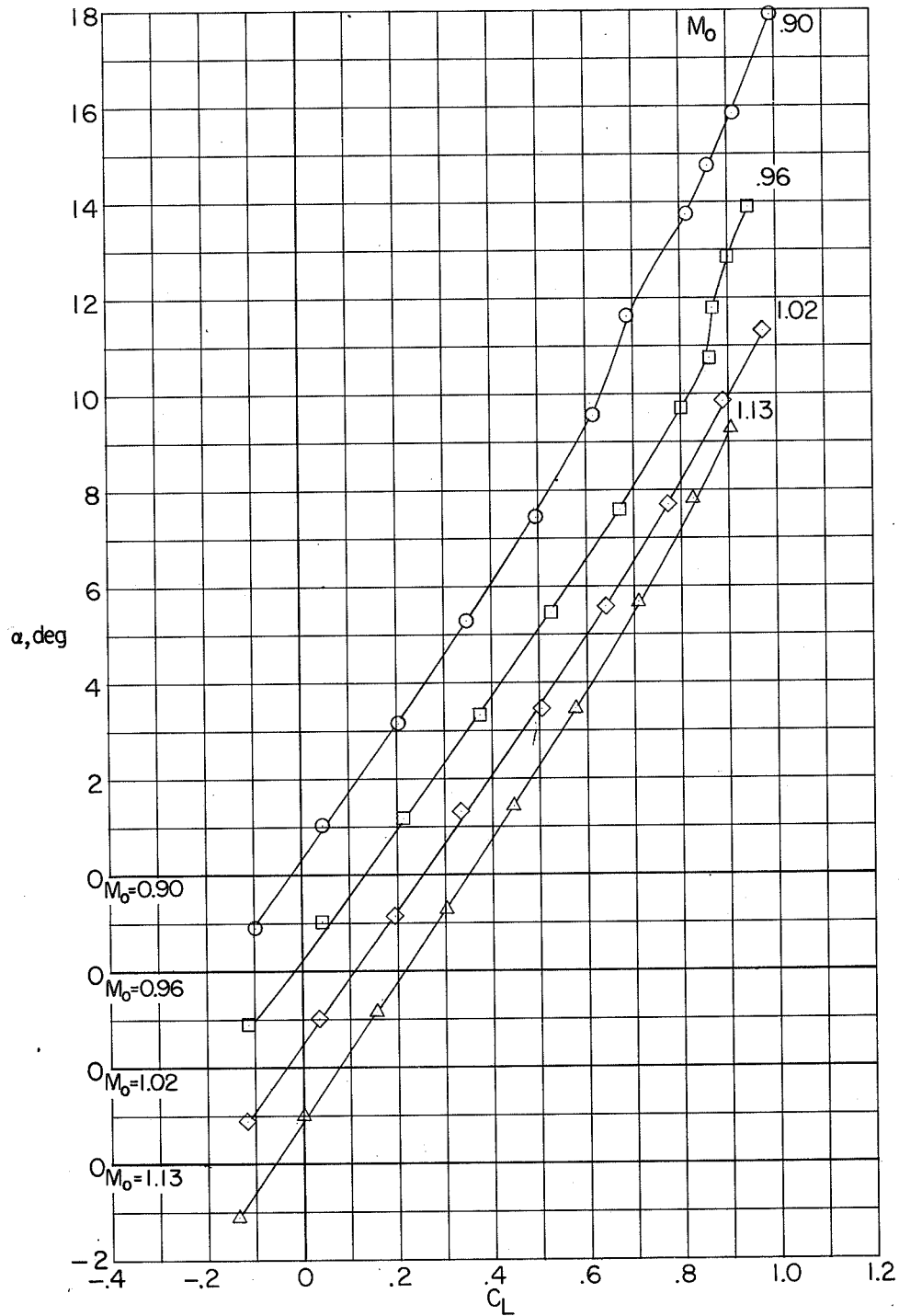
(b) Drag coefficient.

Figure 15.- Continued.



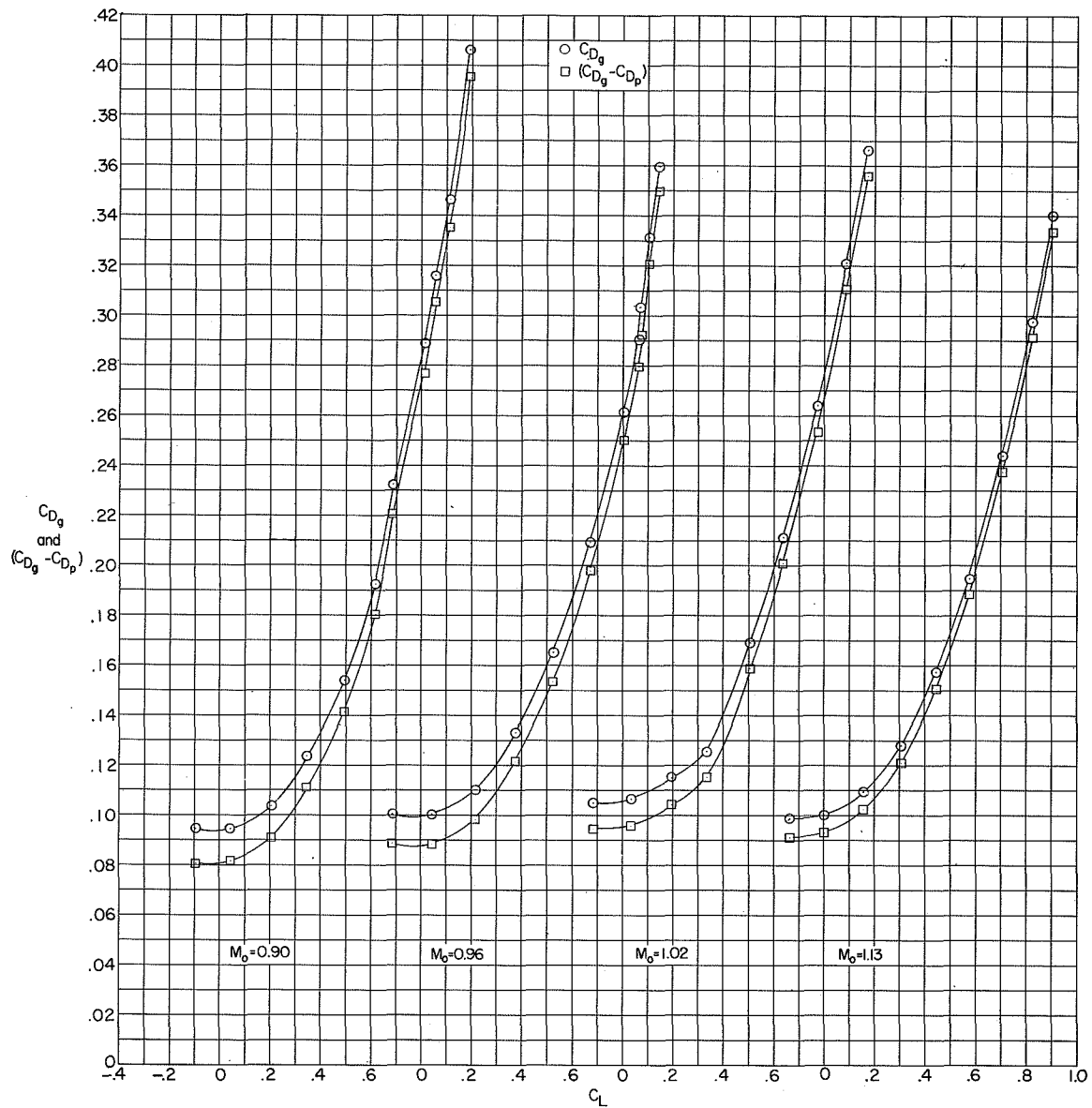
(c) Pitching-moment coefficient.

Figure 15.- Concluded.



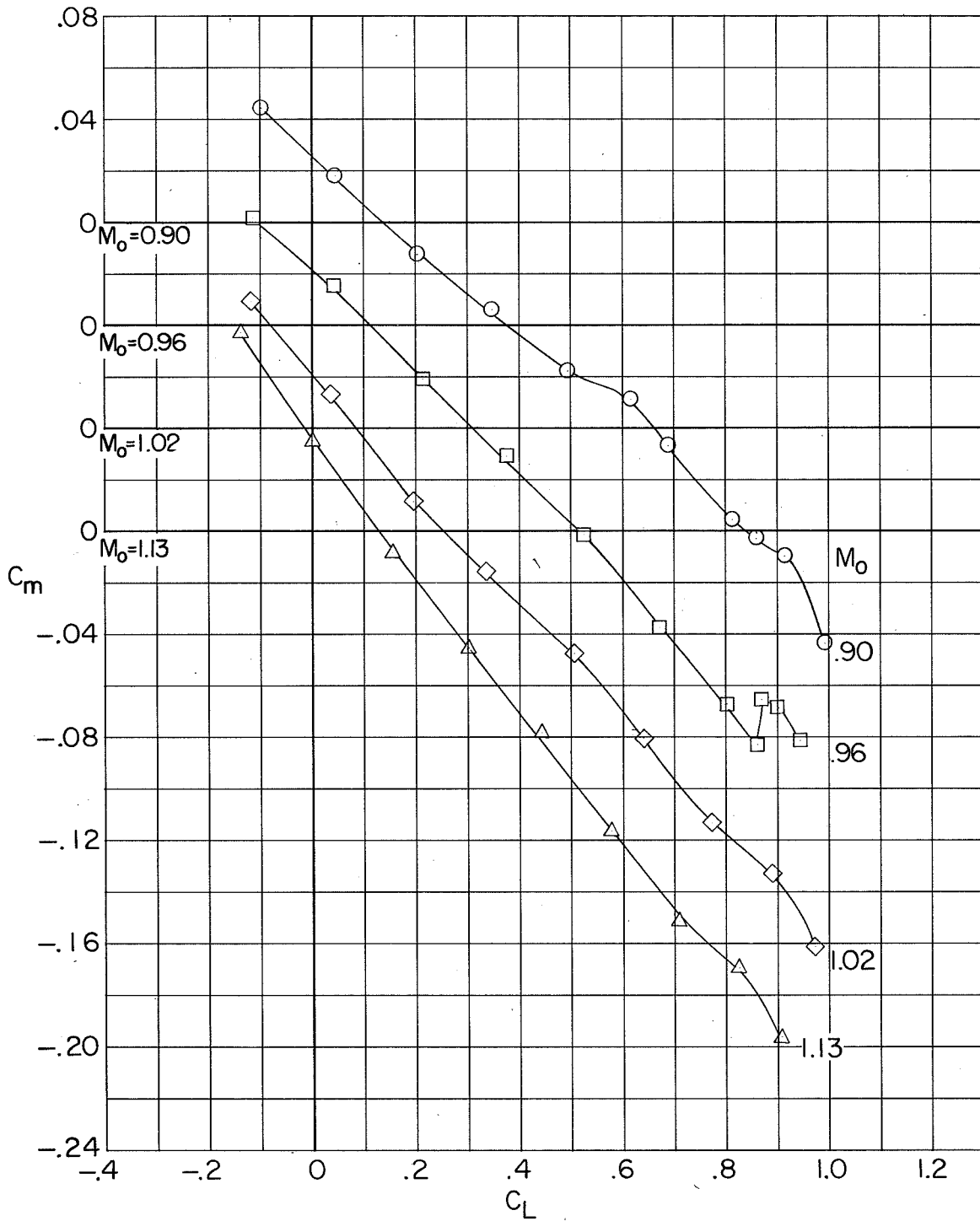
(a) Angle of attack.

Figure 16.- Variation of aerodynamic coefficients with lift coefficient. Complete model plus 45° speed brakes in location 1; $i_t = 0^\circ$; internal flow in model; mass flow rake off.



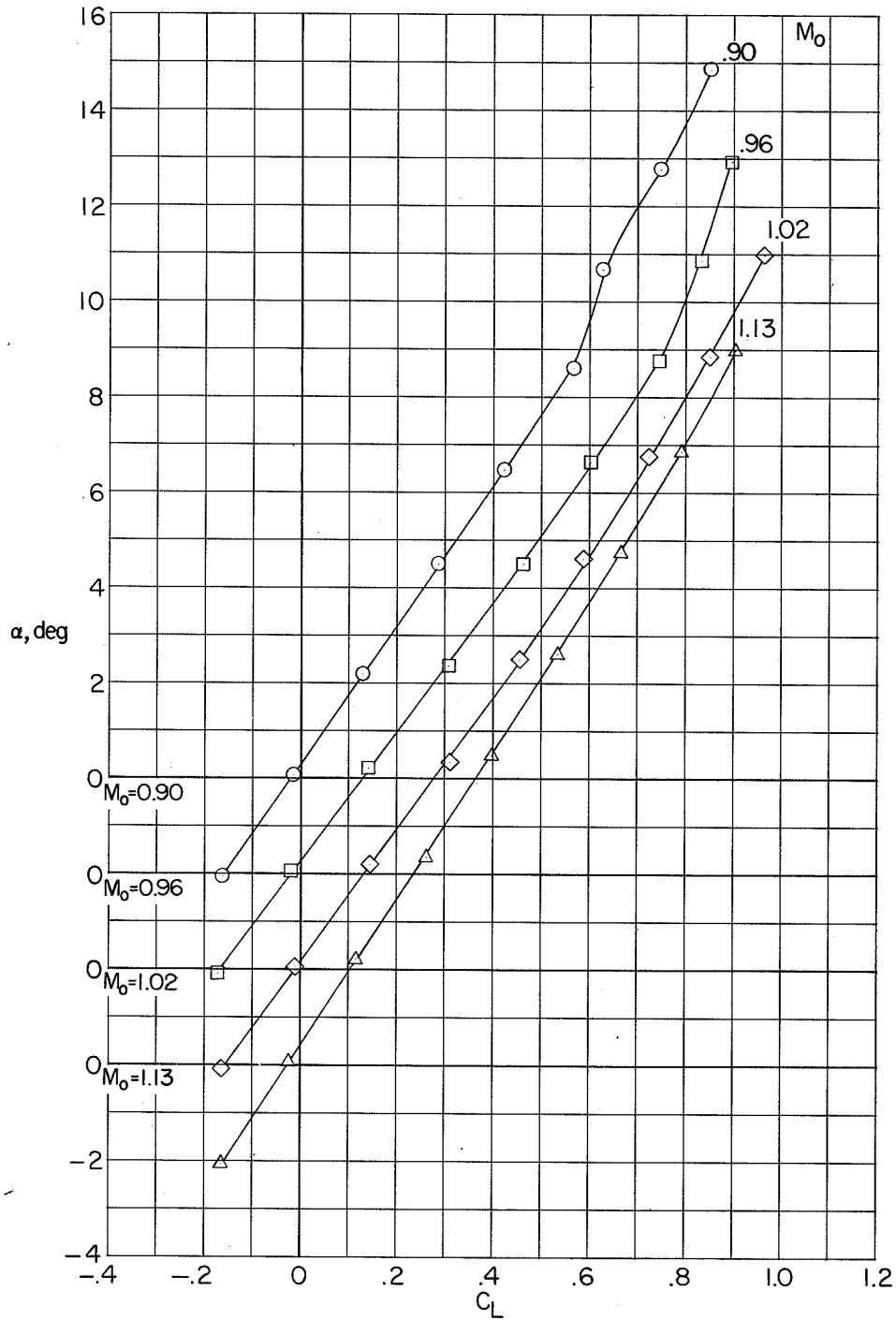
(b) Drag coefficient.

Figure 16.- Continued.



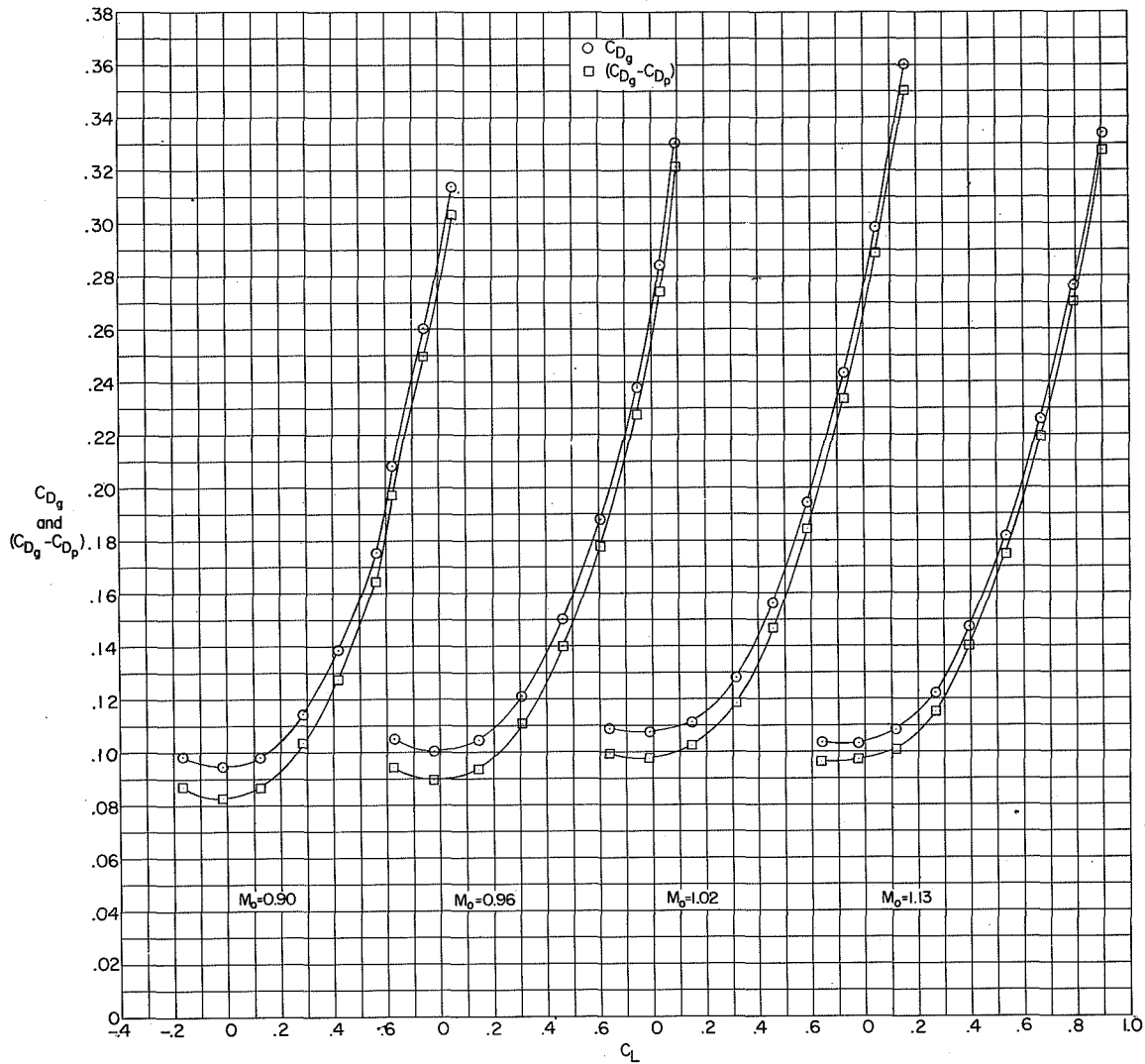
(c) Pitching-moment coefficient.

Figure 16.- Concluded.



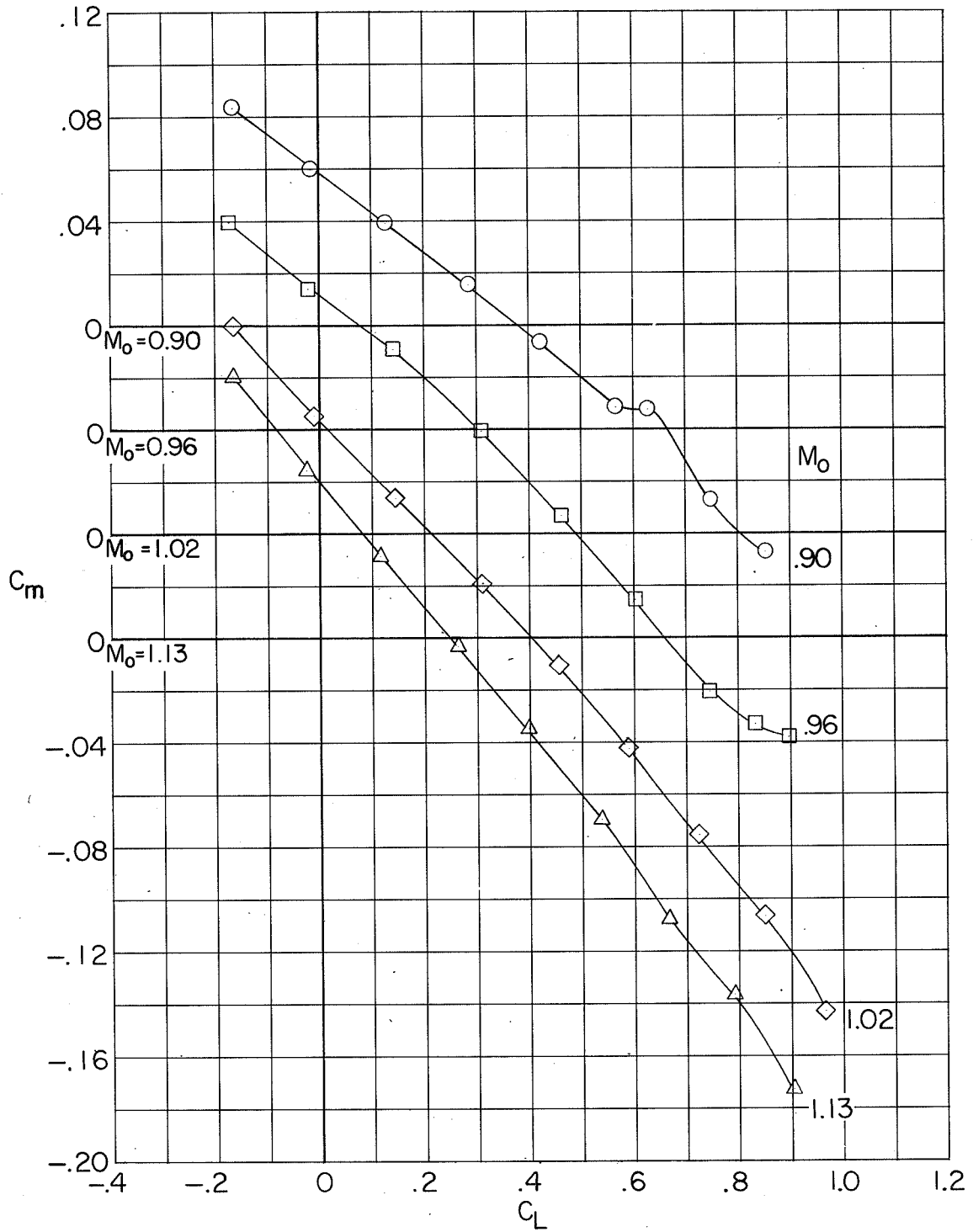
(a) Angle of attack.

Figure 17.- Variation of aerodynamic coefficients with lift coefficient. Complete model plus 45° speed brakes in location 2; $i_t = 0^\circ$; internal flow in model; mass flow rake off.



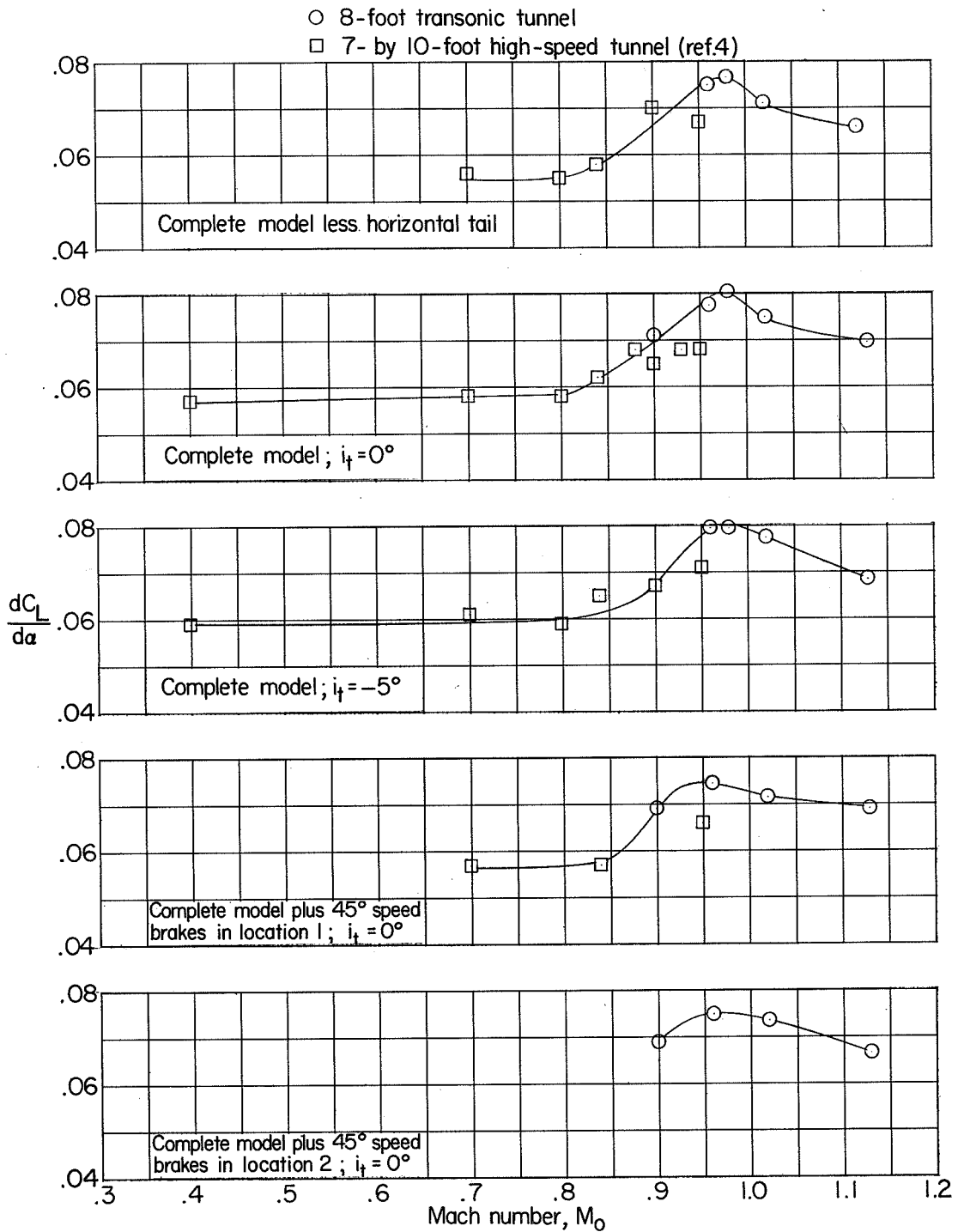
(b) Drag coefficient.

Figure 17.- Continued.



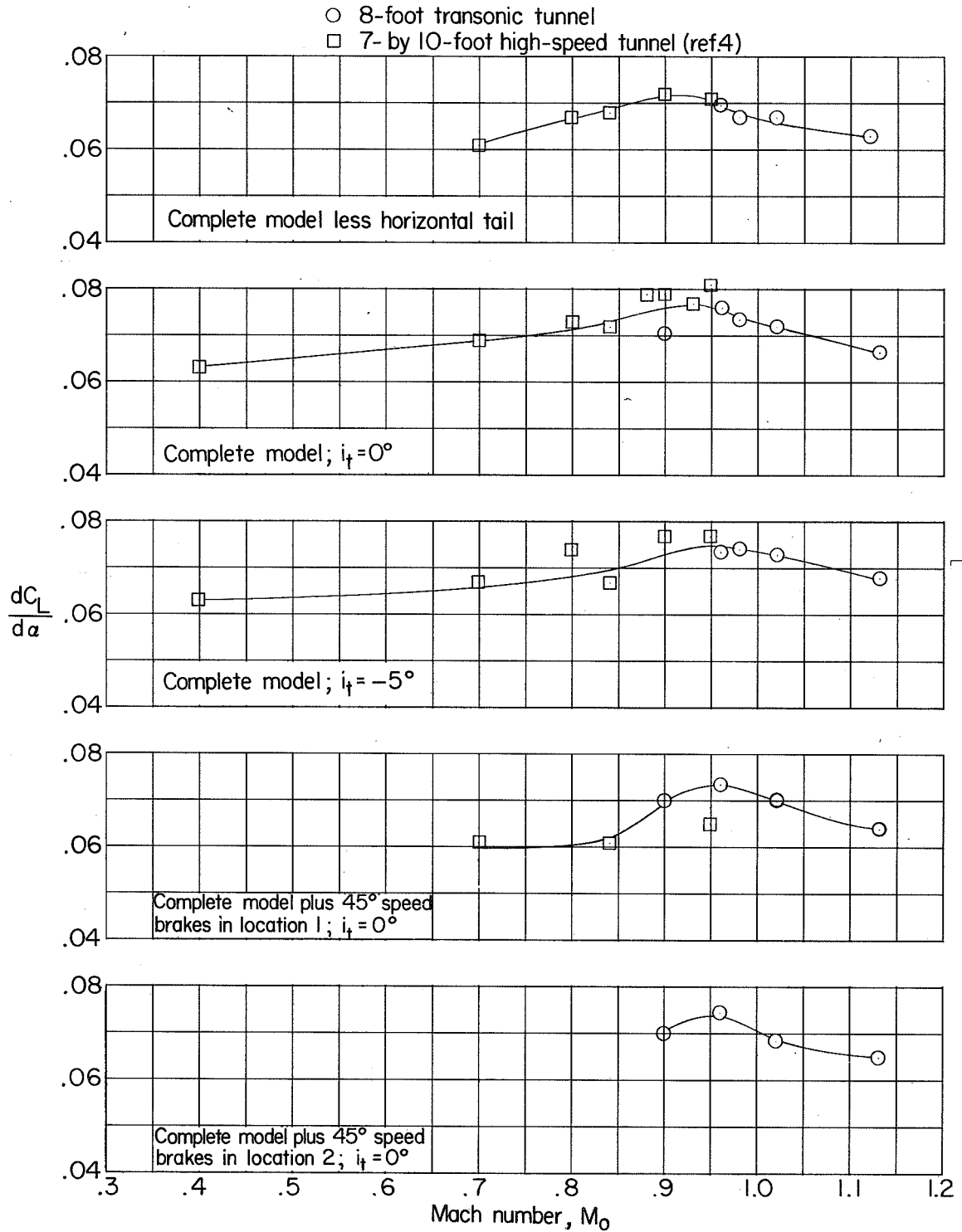
(c) Pitching-moment coefficient.

Figure 17.- Concluded.



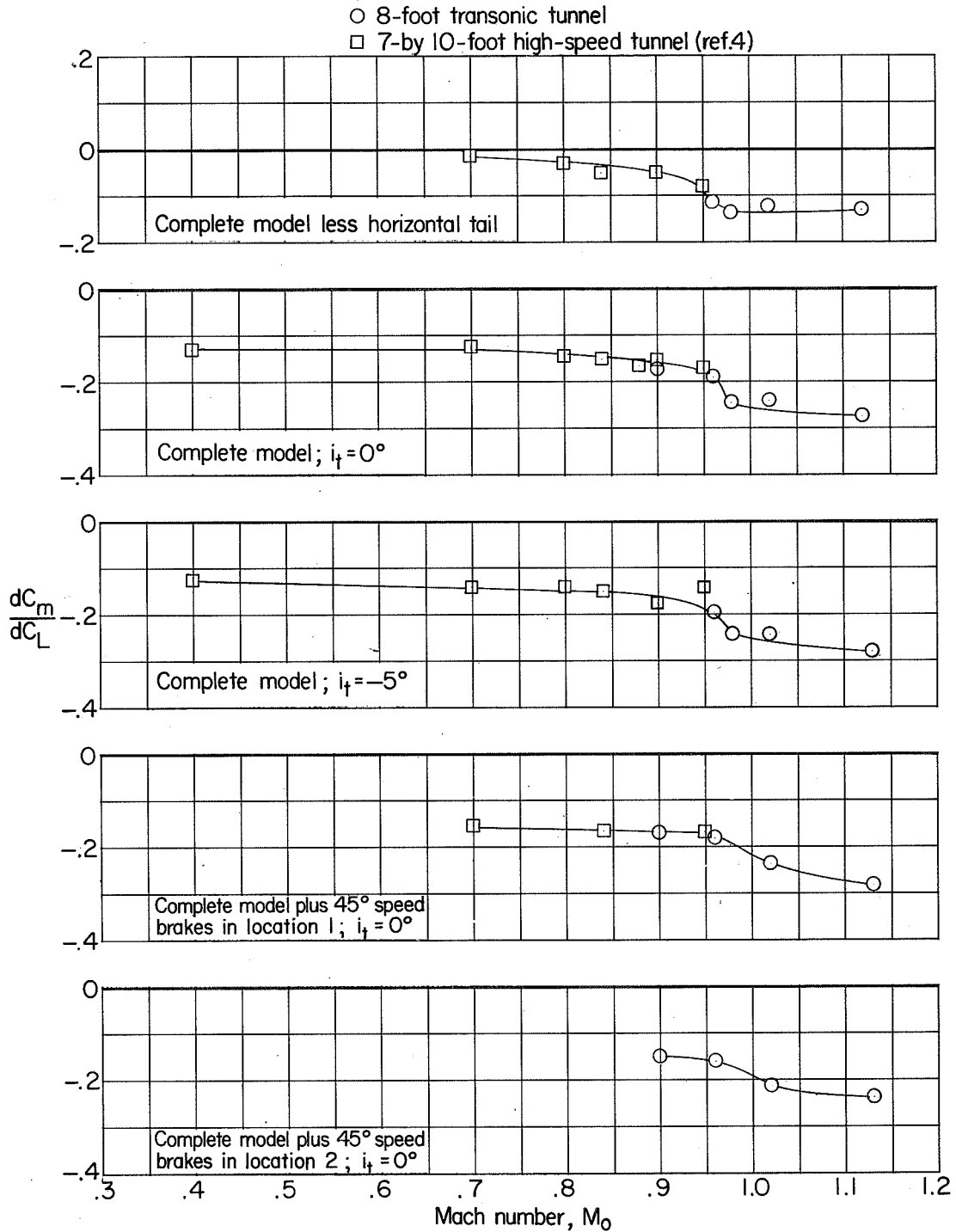
(a) $C_L = 0$.

Figure 18.- Variation of lift-curve slope with Mach number for various configurations. Internal flow in model.



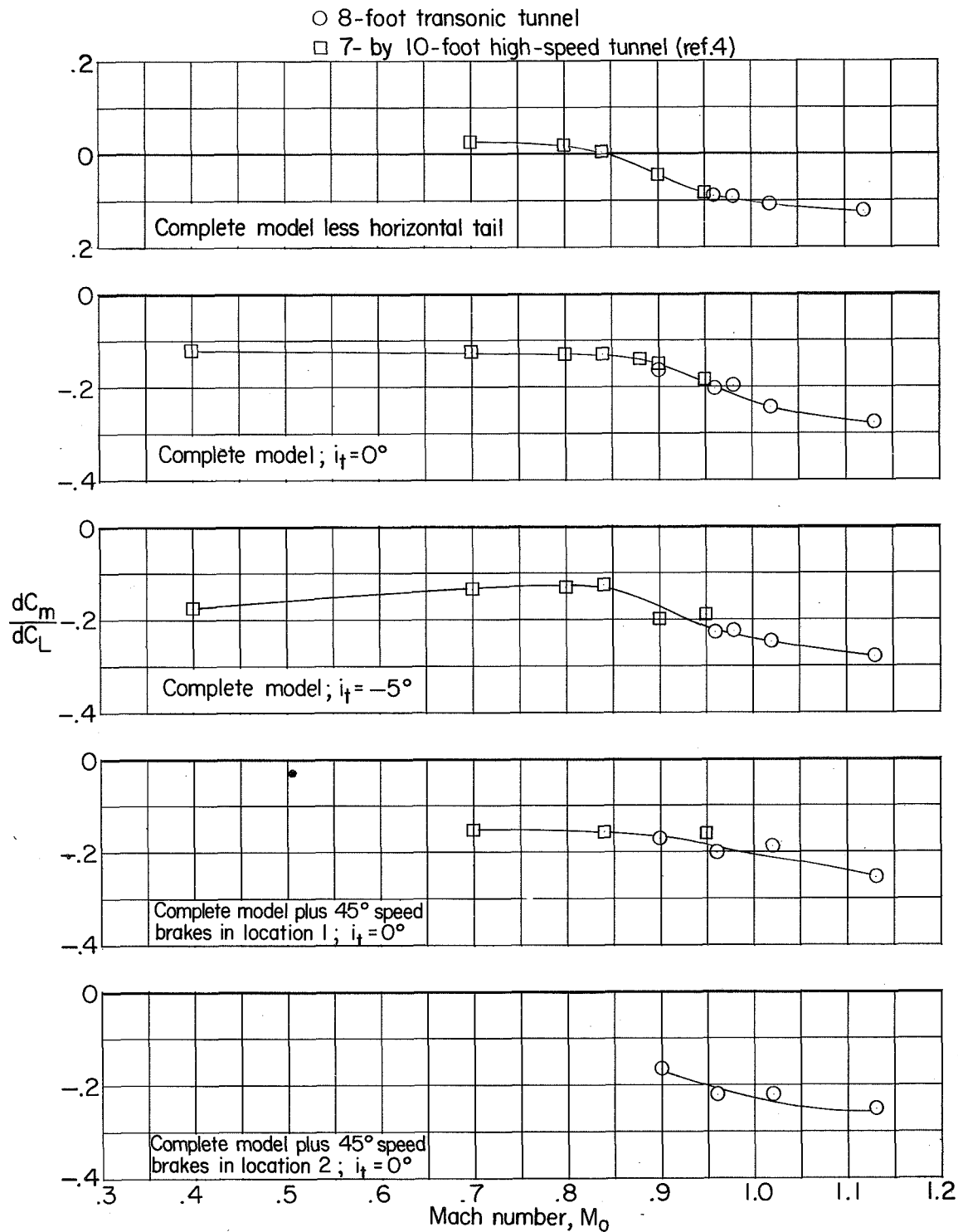
(b) $C_L = 0.4$.

Figure 18.- Concluded.



(a) $C_L = 0$.

Figure 19.- Variation of static-longitudinal-stability derivative with Mach number for various configurations. Internal flow in model.



(b) $C_L = 0.4$.

Figure 19.- Concluded.

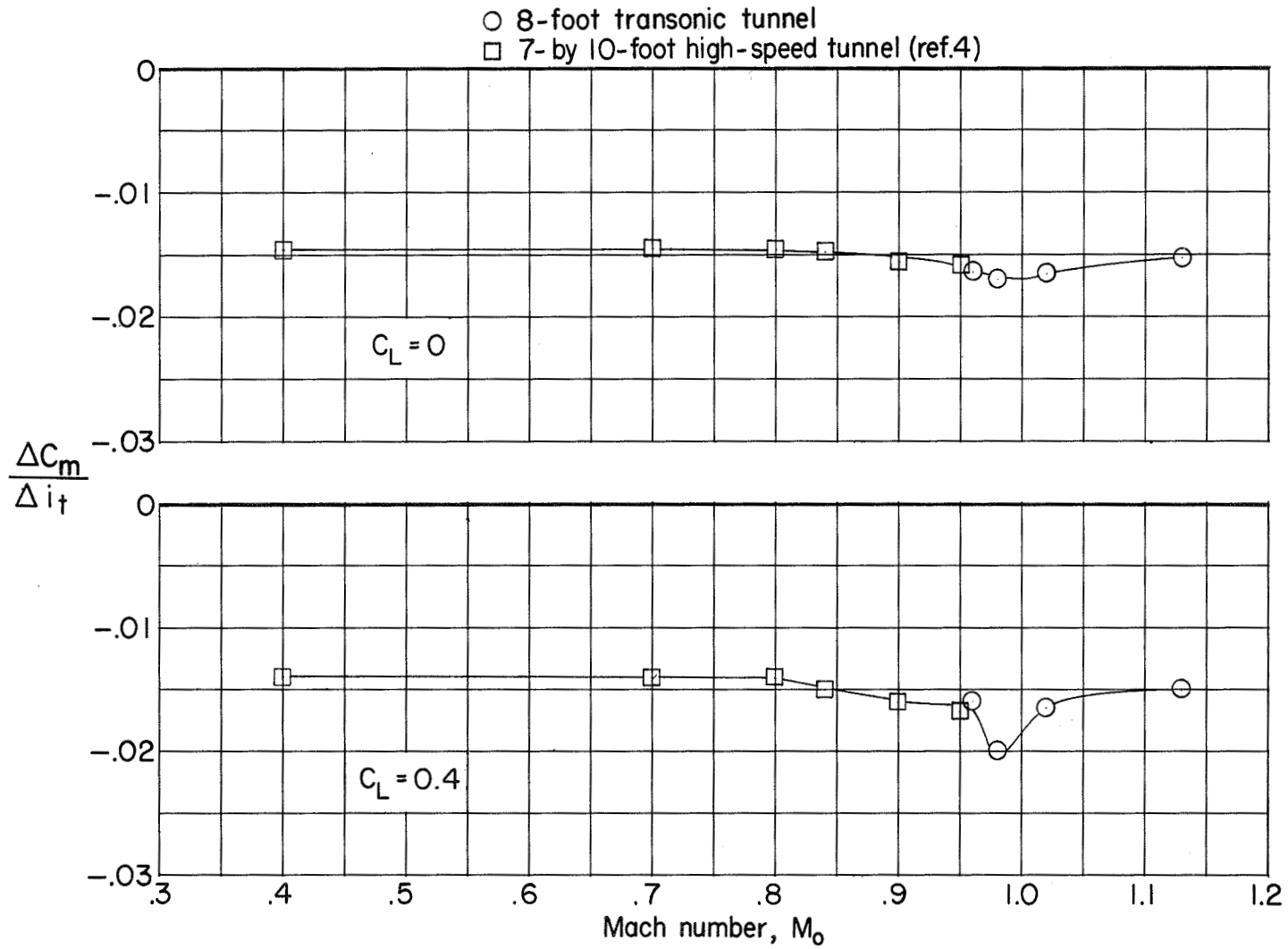
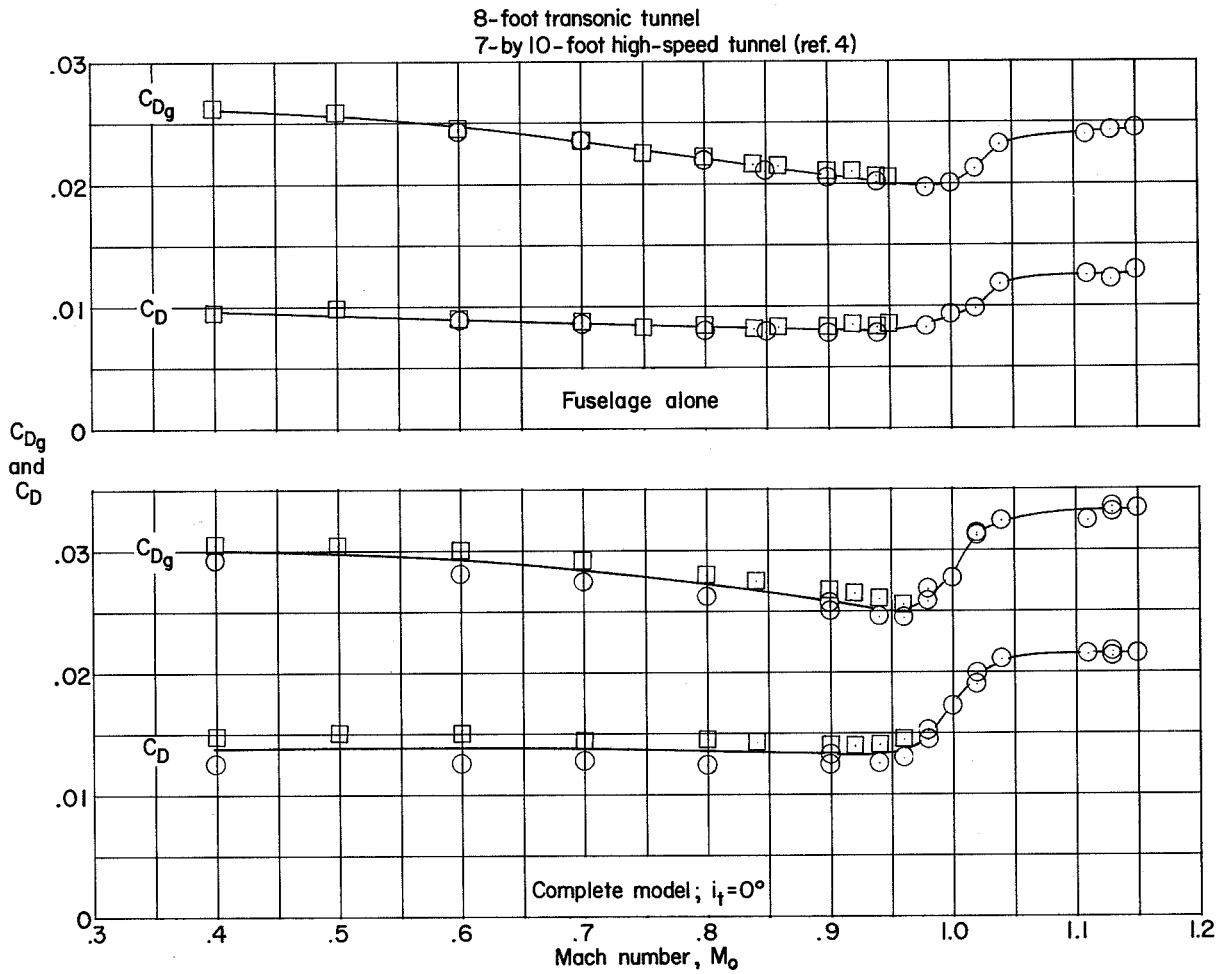
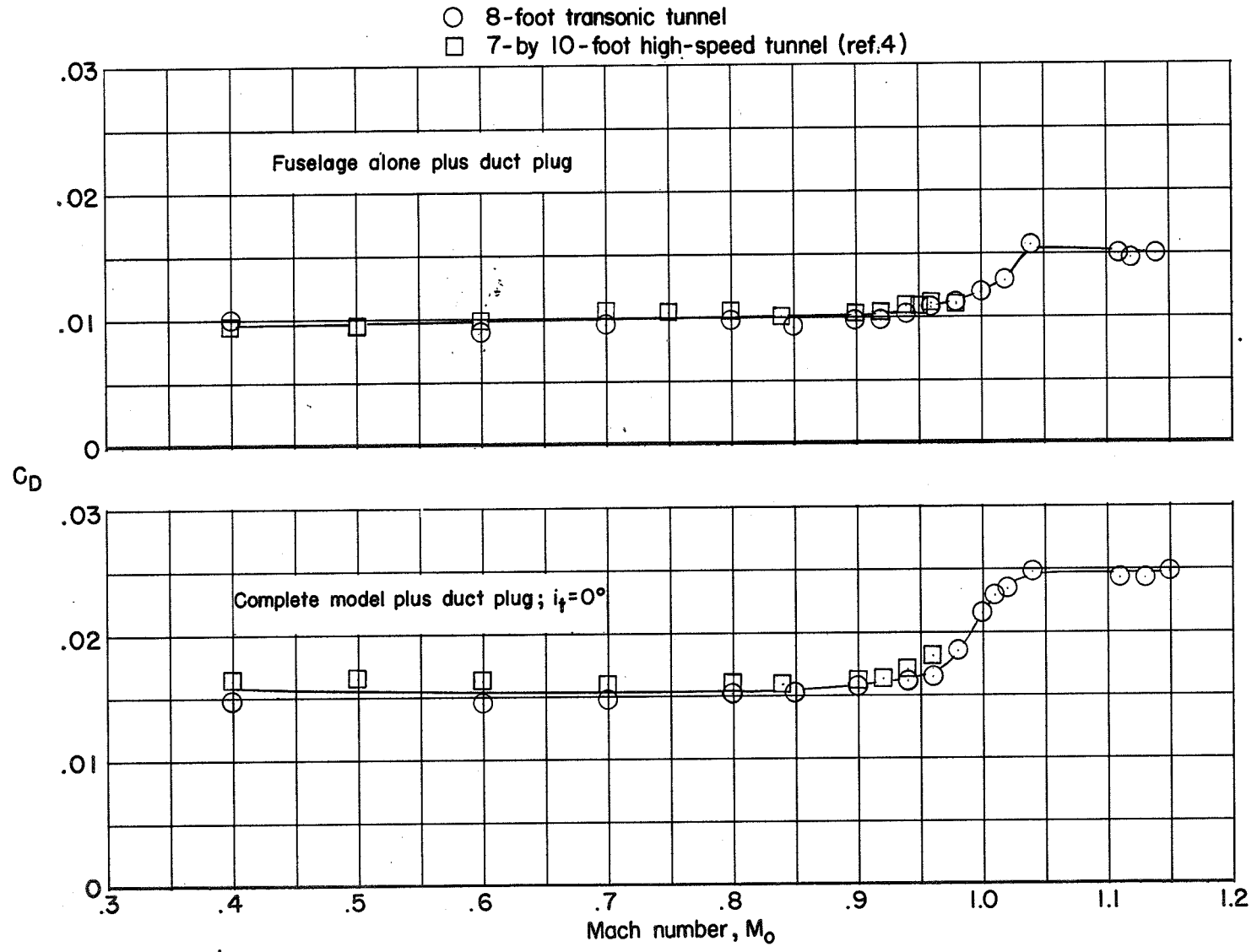


Figure 20.- Variation of horizontal-tail effectiveness with Mach number.
 Complete model; internal flow in model.



(a) Internal flow in model.

Figure 21.- Variation of drag coefficient with Mach number for various configurations. $\alpha = 0^\circ$.



(b) No internal flow in model.

Figure 21.- Concluded.

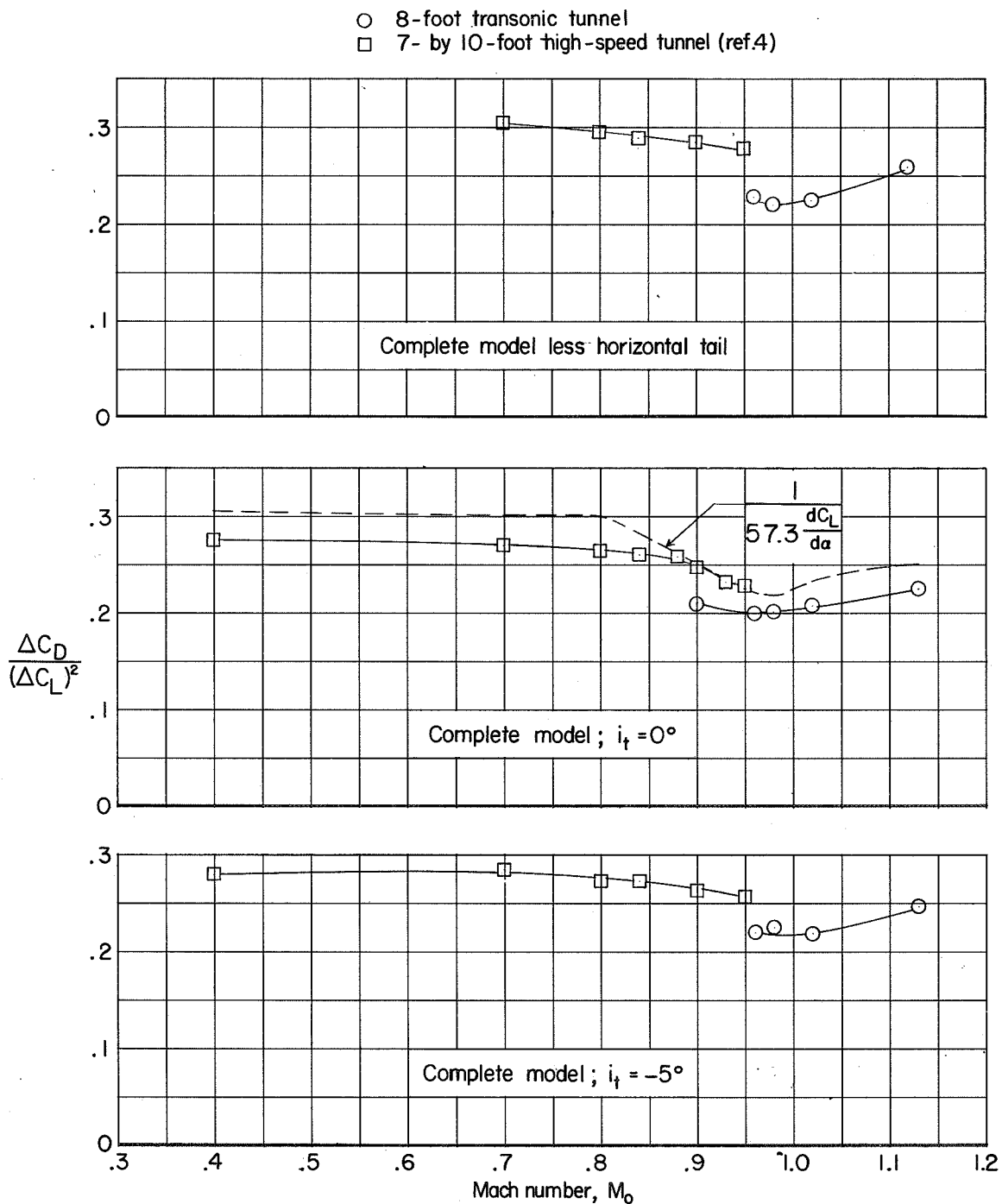


Figure 22.- Variation of drag-rise factor with Mach number for various configurations. Internal flow in model.

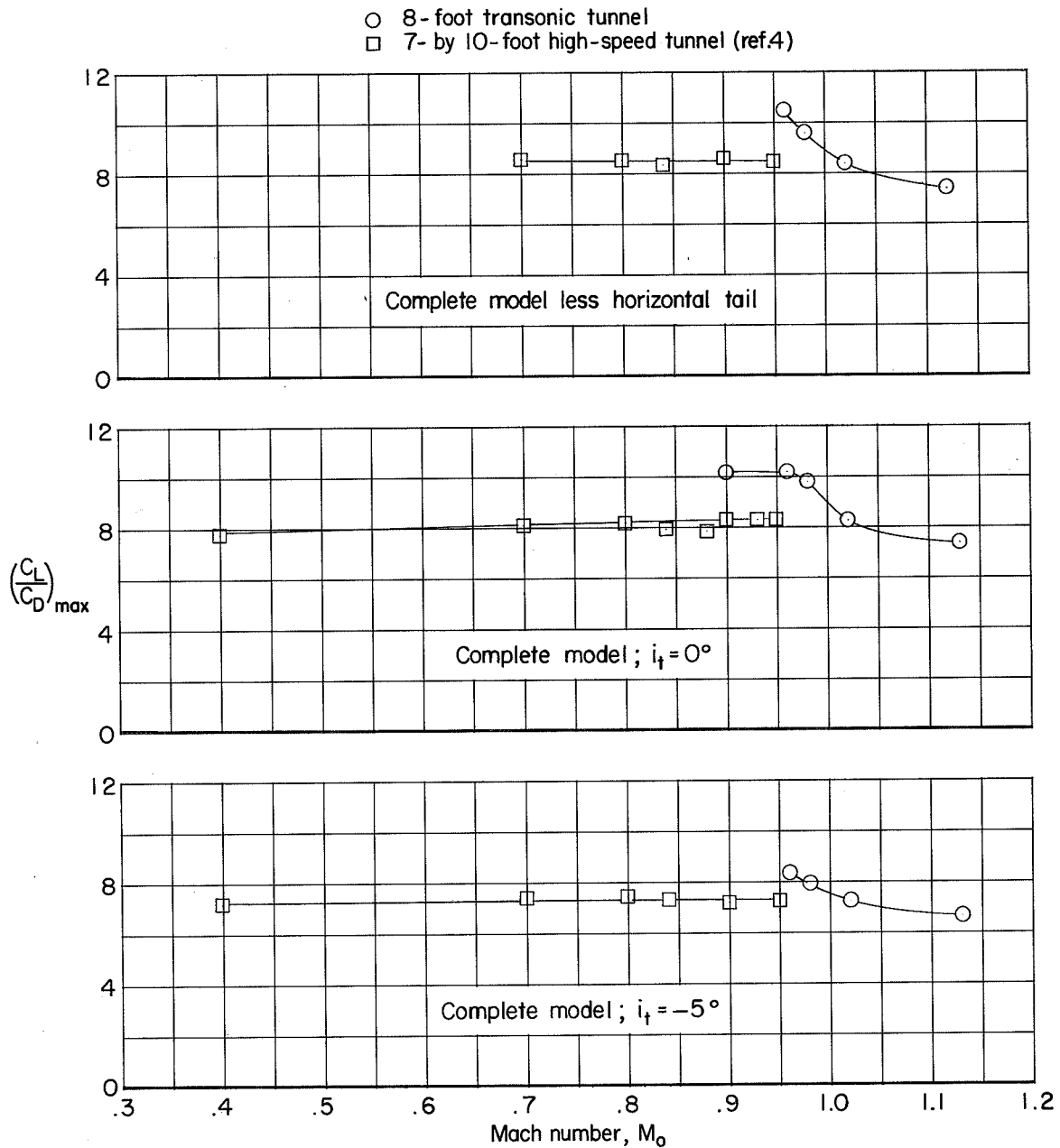


Figure 23.- Variation of maximum lift-drag ratio with Mach number for various configurations. Internal flow in model.

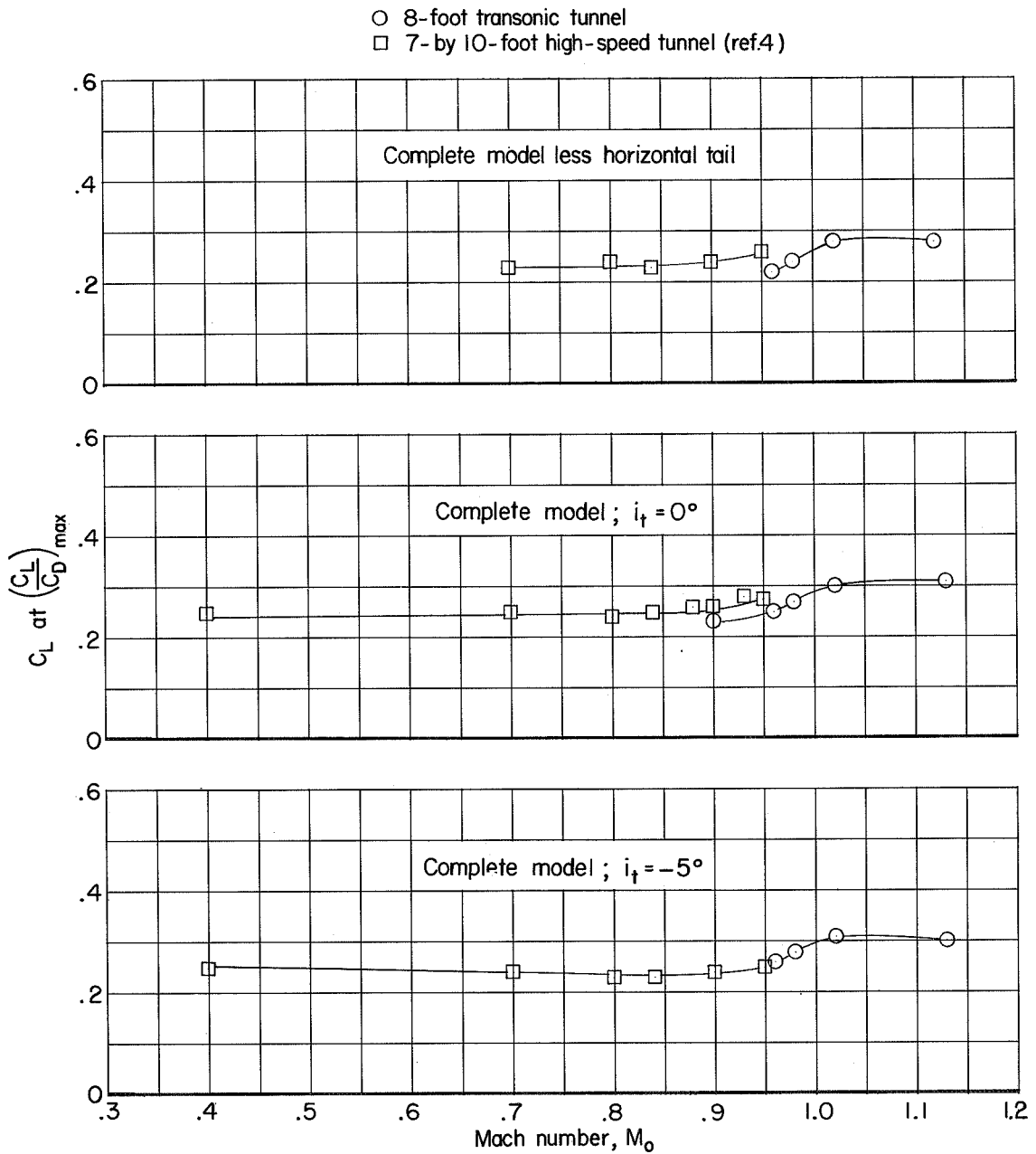


Figure 24.- Variation with Mach number of lift coefficient corresponding to maximum lift-drag ratio for various configurations. Internal flow in model.

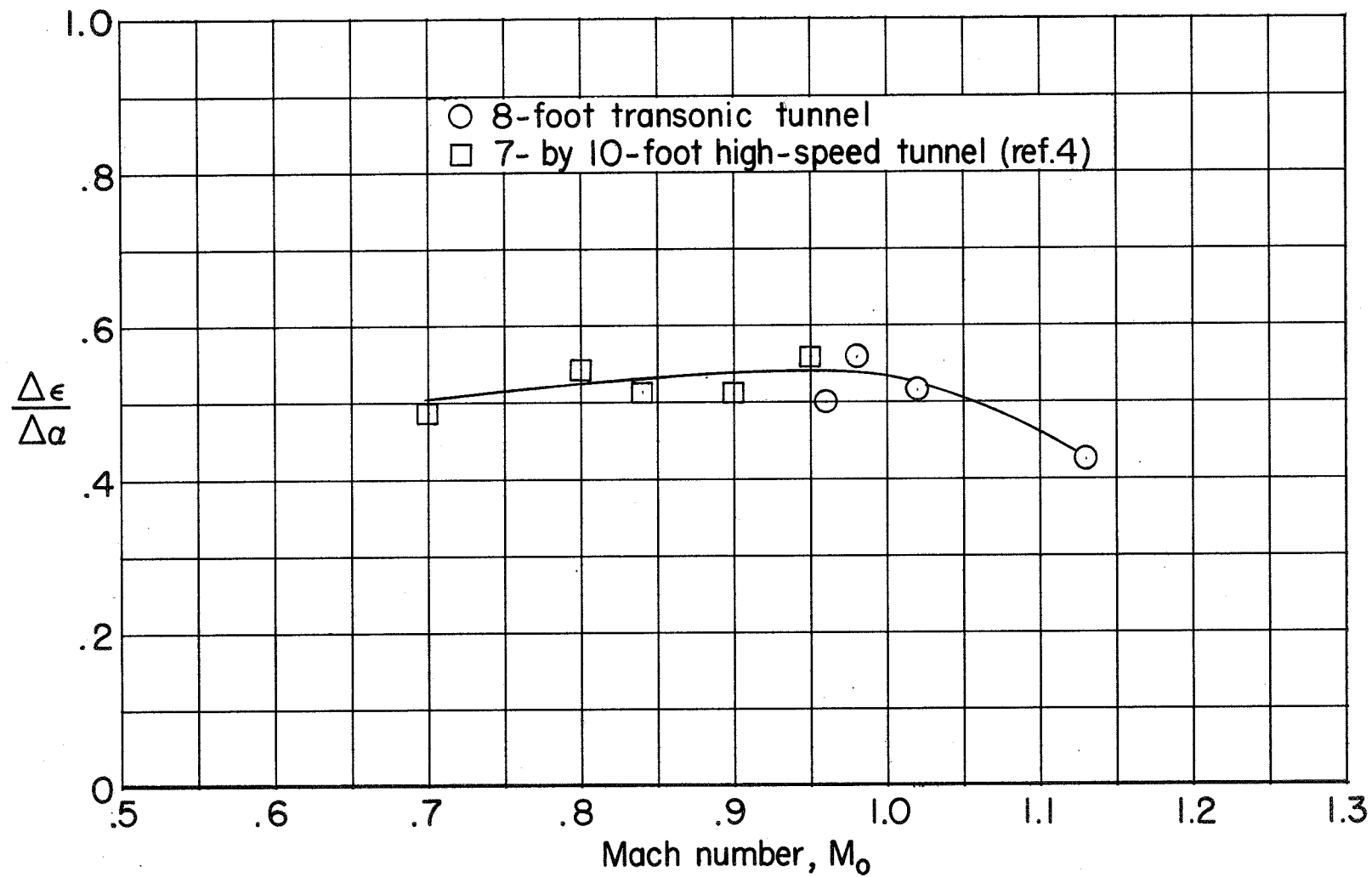
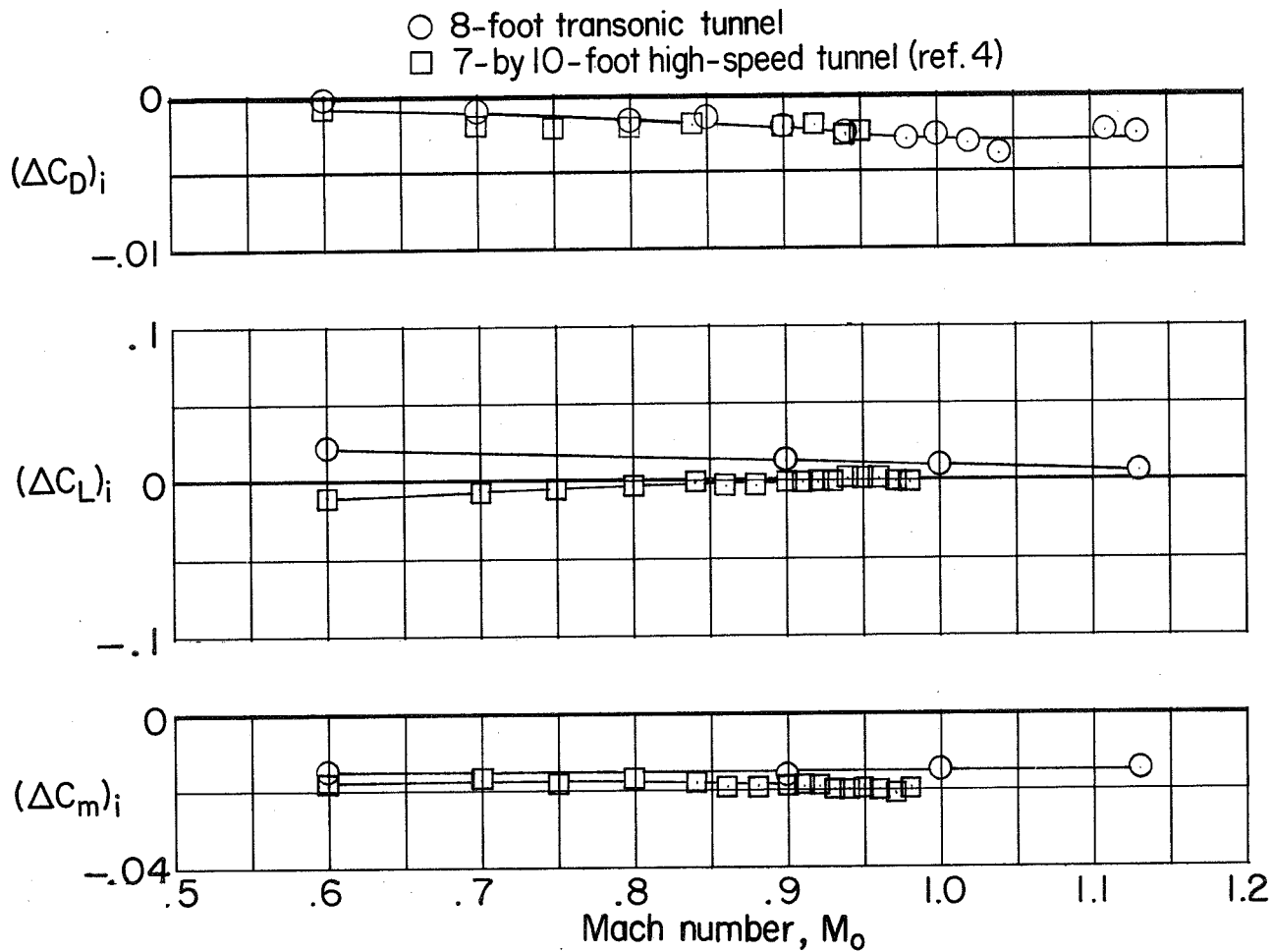
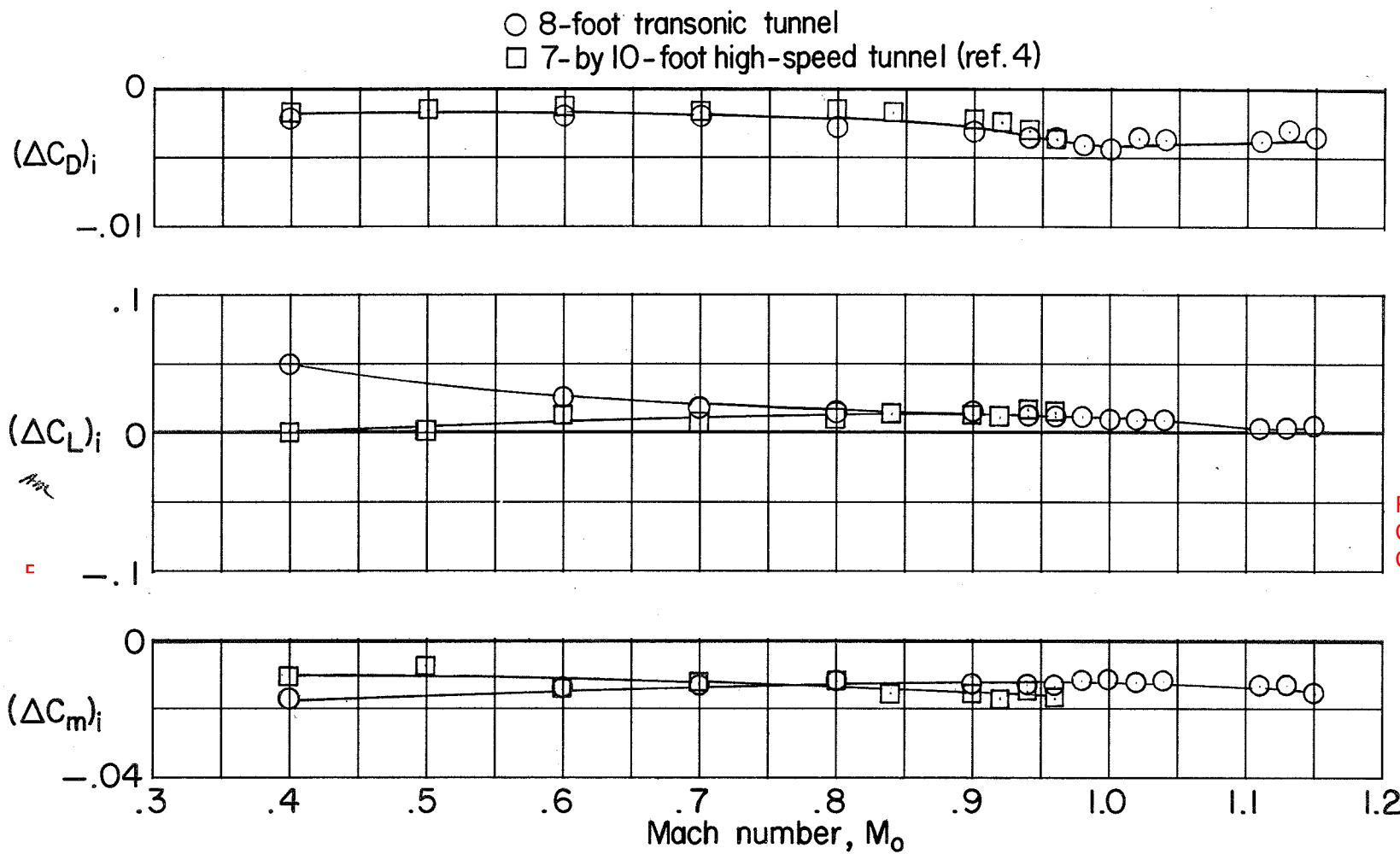


Figure 25.- Variation of effective downwash factor with Mach number.
Complete model. Internal flow in model.



(a) Fuselage alone.

Figure 26.- Incremental effect of internal flow on aerodynamic characteristics. $\alpha = 0^\circ$.



RESTRICTION/
 CLASSIFICATION
 CANCELLED

(b) Complete model; $i_t = 0^\circ$.

Figure 26.- Concluded.

RESTRICTION/
 CLASSIFICATION
 CANCELLED